QATAR UNIVERSITY

COLLEGE OF ENGINEERING

RADIATION-FREE IMAGING FOR DISTAL HOLE TARGETING IN INTRAMEDULLARY NAILING

BY

MONTHER GHAFEL ABU-GAOUD

Thesis Submitted to the Faculty of the

College of Engineering

in Partial Fulfillment

of the Requirements

for the Degree of

Masters of Science in Electrical Engineering

June 2017

COMMITTEE PAGE

The members of the Committee approve the Thesis of Monther Ghafel Abu-Gaoud defended on [Defense Date].

_____

Dr. Fadi Jaber
Thesis Supervisor

_____

Dr. Faycal Bensaali
Thesis Supervisor

Approved:

_____

Khalifa Al-Khalifa, Dean, College of Engineering

ABSTRACT

ABU-GAOUD, MONTHER, GHAFEL, Masters: January : 2017,

Masters of Science in Electrical Engineering

Title: Radiation-Free Imaging for Distal Hole Targeting in Intramedullary Nailing

Supervisor of Thesis: Dr. Fadi Jaber, Dr. Faycal Bensaali.

Orthopedic surgeons are routinely faced with long-bone fractures. Their preferred surgical procedure for dealing with such cases is Intra-Medullary Nailing (IMN). The aforementioned surgery usually involves alignment of the fractured fragments of the long-bone followed by the insertion of a nail down its medullary canal. To prevent displacement of bone fragments, locking screws are inserted through the proximal and distal bone fragments into holes located at the proximal and distal regions of the nail. The most challenging part of IMN surgery is the location of the two distal holes of the nail after insertion, termed *distal hole targeting*. To find the exact location of the distal holes, several methods have been developed. The most popular method is the *free-hand technique* which involves the acquisition of radiographic images of the bone and nail to find the holes.

The objective of this thesis is to review the current state of the art regarding distal hole targeting and investigate the possibility of developing an alternative imaging

technique for finding the distal holes that will be free of ionizing radiation. More specifically, this work concentrates on characterizing the suitability of Earth's Field Nuclear Magnetic Resonance (EFNMR) for this particular application. The characterization of this imaging method is performed through a series of experiments. The investigated solution poses several major challenges like contrast between different regions, time consumption, and detecting NMR signals in less than 19 ml water volume. The first two problems are resolved by using a contrast agent, Copper (II) Sulfate ($CuSO_4$), which decreases the relaxation time by 6-7 times. In effect, this has decreased the experimental time. For instance, the experimental time was reduced from 8.32 min to 1.36 min. For the third challenge where the target is to detect the signal for 1.8 ml, all the proposed solutions have not worked as expected.

DEDICATION

I would like to dedicate this work to my mother, Ameera Al-Surkhi, for her support and prayers. My father, Ghafel Abu-Gaoud, would be very proud of me if he is alive today. God bless his soul.

To my loving wife, Elham Al-Saqa, and all my children, Qais, Abdel-Rahman, Fares, and my little daughter Ameera, thank you for your patience and understanding. I was able to balance family time and study time together with your help.

ACKNOWLEDGMENTS

The completion of this undertaking could not have been possible without the participation and support of many people whose names may not all be enumerated here. Their contributions are sincerely appreciated and grateful acknowledged. However, I would like to express my deep appreciation particularly to the following:

Dr. Fadi Jaber, my supervisor QU.

Dr. Faycal Bensaali, my supervisor QU.

Mr. Baker Buduan, Chemistry and Earth Science Dept QU.

Dr. Hassan I.Nimir, Chemistry and Earth Science Dept QU.

Dr. Mammon Abu Samhadan, Hamad Medical Corporation (HMC).

Dr. Talal Ibrahim, (HMC).

Mr. Maher Ashawakhfa, (HMC).

TABLE OF CONTENTS

LIST OF FIGURES

LIST OF TABLES

1 INTRODUCTION

1.1 Thesis Significance and Objectives

The treatment of long bone fractures like tibia, humerus and femur shown in Figure 1.1 has always been a debate and a subject of controversy. Many surgical interventions are available like *Intra-Medullary Nailing (IMN), External Fixation* and *Plate Fixation,* however, IMN is the most popular technique and is considered as the standard treatment method for long bone fractures [1-18]. Statistics show that approximately 39% out of the total fracture cases admitted to hospital are femur fracture. Whereas, 15% and 11% of the total fracture cases admitted to hospital are humerus and tibia fractures respectively [12].

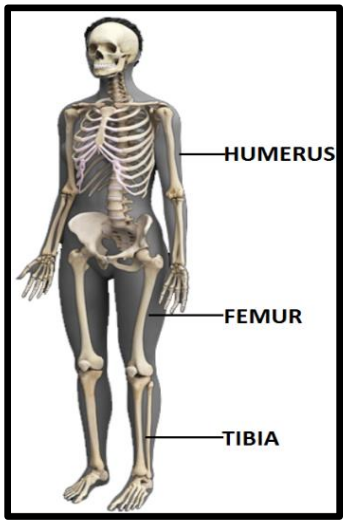

Figure 1.1. Example of major long bones in the Human Skeletal System [19].

The IMN technique was discovered and developed by Gerhard Kuntscher in 1940 [10]. In this surgical operation, a tubular metal nail was inserted from the proximal part of the long bone passing through the medullary canal and the fracture part to the distal part to stabilize the upper and lower parts of the bone as well as the fracture itself. Figure 1.2 illustrates the technique. The advantages of IMN over other surgical interventions: are shorter hospitalization time, quicker healing of the fracture, and good alignment of broken bone parts that leads to less fracture shortening [7, 20]. When the nail is inserted into the intramedullary canal it is fixed using screws from the upper part (proximal part) and the lower part (distal part). The Proximal screw fixation part is straightforward and can be completed by using a mechanical guide. For the distal part, the same procedure cannot be performed due to the nail deformation during insertion into the medullary canal [15, 21]. Images (usually x-rays) are required to locate and drill holes at the site of distal holes of nail [15, 16]. This will prevent trial and error fixation, inadequate fixation, and bone cracking since the bone becomes brittle when multiple holes are drilled.

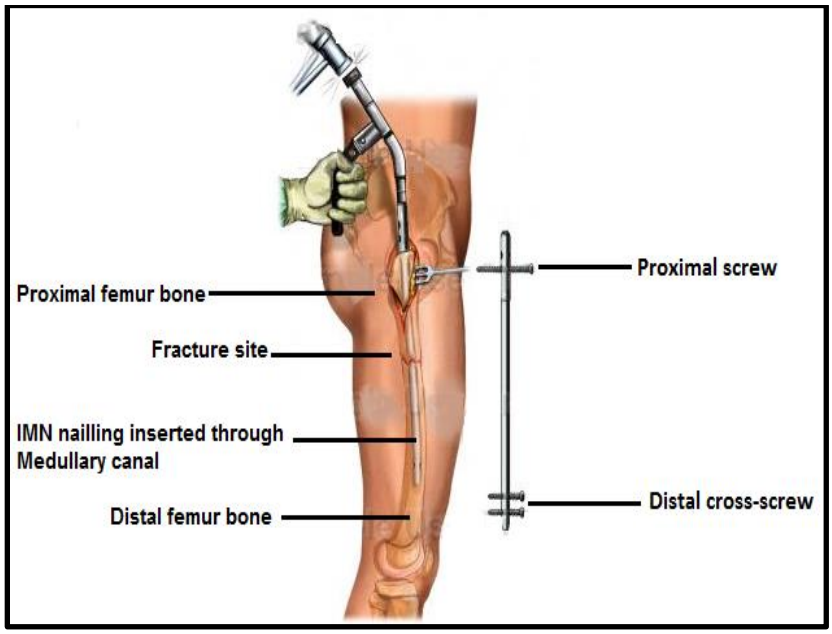

Figure 1.2. Lateral side showing the femur bone, sample of IMN under insertion process [22].

In terms of finding the exact location of distal holes of the nail, several methods and devices have been developed. The most popular method is the free-hand technique [1, 3-9, 11, 13-18] that helps the surgeon to detect the exact location and orientation of distal holes. In spite of the fact that this method is accurate and preferred by surgeons, it is risky for the patient and the medical team due to exposure to ionizing radiation. The number of fluoroscopic images required for distal screw locking is 17 to 52 images [18]. Other methods which are radiation-free or low radiation are also being investigated such as: magnetic flux based [23, 24], mechanical [17], computer-assisted [8, 9, 15, 16], and lighting [5]. All of these techniques have advantages and disadvantages and they will be discussed in Chapter 2.

The work presented in this thesis is to develop an alternative imaging technique for locating the distal holes of nail, the alternative imaging technique is ionizing radiation-free, in order to protect patients and surgical team who are performing the IMN procedure. The imaging technique that will be investigated is Earth's Field Nuclear Magnetic Resonance (EFNMR). This particular technique is similar to Magnetic Resonance Imaging, however, it does not utilize any large magnetic fields, and therefore, the hazard of a large magnet that could attract metallic objects (e.g., surgical tools and nails) is not there. Furthermore, the following objectives will be addressed in this thesis:

1. Review the literature regarding the available techniques that are used for locating the distal holes of IMN nails (Chapter 2).
2. Obtain, install, and test an EFNMR instrument in order to perform distal hole location experiments (Chapter 4 and Chapter 5).
3. Develop a Femur Bone Model with a medullary canal and nail that will be used in experiments for validating the proposed imaging technique (Chapter 6).
4. Perform validation experiments using the proposed imaging technique (Chapter 6).
5. To evaluate the suitability of EFNMR for imaging the distal holes of IMN, and to prove if the concept of this method works or not (Chapter 6).
6. To compare the EFNMR against the state of the art in terms of more reliable and time (Chapter 2, 6 and 7).

1.2 Thesis Timeline Chart

Figure 1.3 illustrates the tasks and timeline plan for the project. The work is divided into six major tasks:

1. Medical/Theory Background and Literature Review.
2. System setup and initial experiments.
3. Nuclear Magnetic Resonance (NMR) experiments.
4. MRI experiments.
5. Testing and validating the EFNMR the femur Bone Model.
6. Final results and thesis writing.

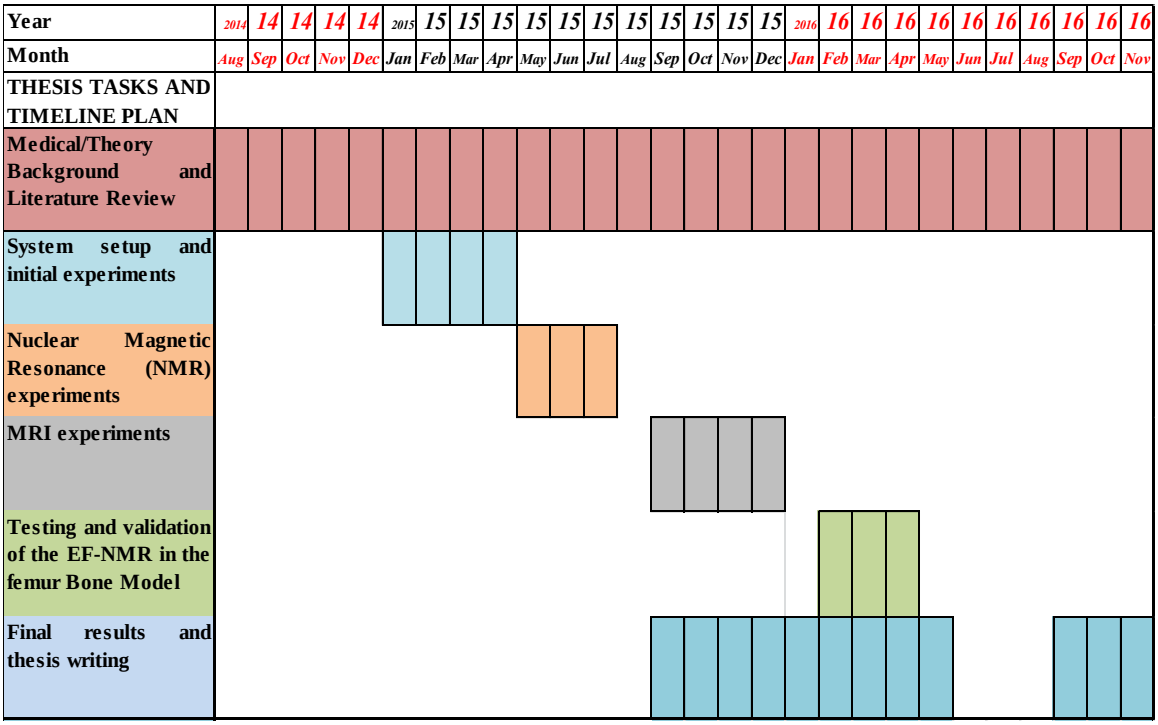

Figure 1.3. Thesis timeline' chart.

1.3 Thesis Structure

The rest of the thesis is as follows: Chapter 2 includes the medical background and types of fractures. It also describes the IMN surgery with emphasis on the distal hole locking part of the operation. The different methods for distal hole targeting are reviewed in this chapter. Chapter 3 introduces the theory of Nuclear Magnetic Resonance (NMR) and Magnetic Resonance Imaging (MRI). Chapter 4 provides an overview of the EFNMR apparatus and its parts along with a detailed description of the important parameters in the NMR and MRI experiments. Chapter 5 presents the experiments for NMR, improvement of the FID signal and shimming, and the measurement of T_2 and T_1. Chapter 6 presents the experiments for MRI and a simple nail-bone-tissue model that can be used for MRI imaging experiments for locating the distal holes. Finally, Chapter 7 concludes the thesis and recommends future directions for this project.

2 LITERATURE REVIEW

This chapter includes the etiology of femur shaft fractures and the IMN technique. The femur fracture is used as an example for IMN because it is the largest bone and is covered by a large amount of muscles and tissues [6]. If a certain technique succeeds in distal locking in the femur, it will definitely succeed for any long bone. Furthermore, prior works on different distal locking techniques are reviewed. Finally, the different distal locking techniques will be compared.

2.1 The Medical Background of Fractures

The skeletal system provides support and protection for soft body organs and helps with body motion. It also stores fat, calcium, and phosphorus, and produces white and red blood cells. The total number of bones for an adult human is 206 bones. The lower extremities of the skeletal system consist of 62 bones. The femur bones (thigh bones) are the largest, heaviest, strongest and longest tubular bones in the human body shown in Figure 2.1, [25, 26]. The femur shaft is a long, straight part of the femur [26]. Exposure of the femur shaft to high mechanisms of injury can cause fractures. The type of fracture depends on the force of injury and it is rare to treat a Femoral Shaft Fracture (FSF) without surgery. FSF is among the most common major injuries that an orthopedic surgeon will be required to treat [20].

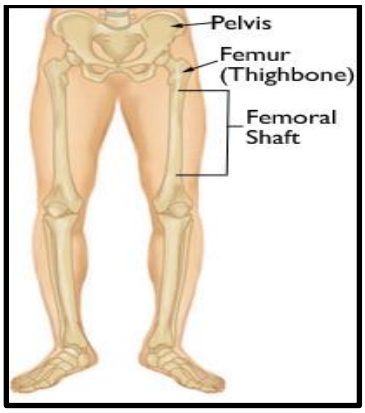

Figure 2.1. Front view shows the femur bone and the femoral shaft [2].

A fracture may occur in the femur's distal, shaft or proximal portion. Traffic road accidents are in charge for 57-74% of all FSF [20]. According to the American Academy of Orthopedic Surgeons (AAOS) femur shaft fractures are classified as, Open (Figure 2.2-A), Transverse (Figure 2.2-B), Spiral (Figure 2.2-C), Comminuted (Figure 2.2-D) and Oblique (Figure 2.2-E) fractures [2].

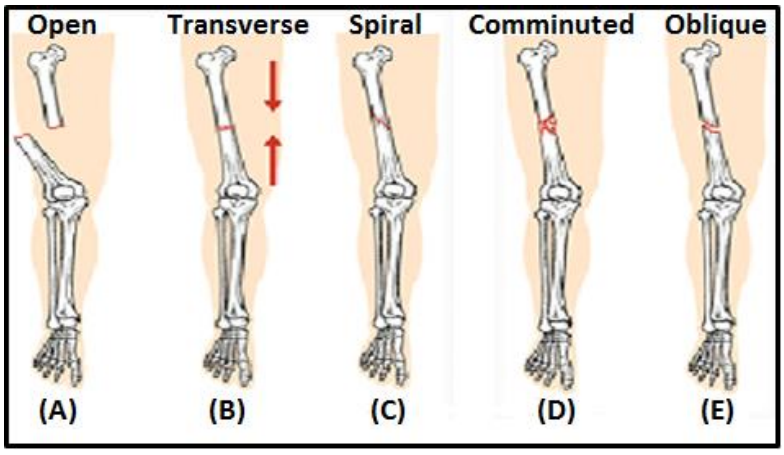

Figure 2.2. FSF types: A) Open. B) Transverse. C) Spiral. D) Comminuted. E) Oblique fractures [27].

Brief descriptions of FSF types are listed in Table 1.

Table 1: FSF types and descriptions

Fracture type	Fracture type description
Open	The fragments are exposed
Transverse	Happens as straight horizontal across the long axis of the shaft femur bone
Spiral	The femur bone exposed to a strong twisting motion and the fracture line encircle
Comminuted	Related to exposure to high energy, the shaft femur fracture breaks to three or more small pieces
Oblique	It is like transverse fracture, but the fracture with angled cross the shaft femur bone

There are many alternative methods to treat the FSF. These are categorized as non-surgical (conservative) methods and surgical methods. Some examples of non-surgical methods are *Traction* and *Cast Bracing*. These methods are rarely used if the surgical treatment methods are available. However, they are still used in developing countries [20]. For surgical methods, examples are Plate Fixation, External Fixation, and IMN, which are illustrated in Figure 2.3. In the Plate Fixation, a metal plate is attached above the outer surface of the fractured bone and fixed by screws. To perform this, a long incision is required by the surgeon. For External Fixation, a metal plate is attached on the outer layer of skin above the femur shaft. This temporary treatment holds the lower and upper fracture site [7, 20]. For IMN method, it is the preferable and first choice for surgeons. It is described more in the next section.

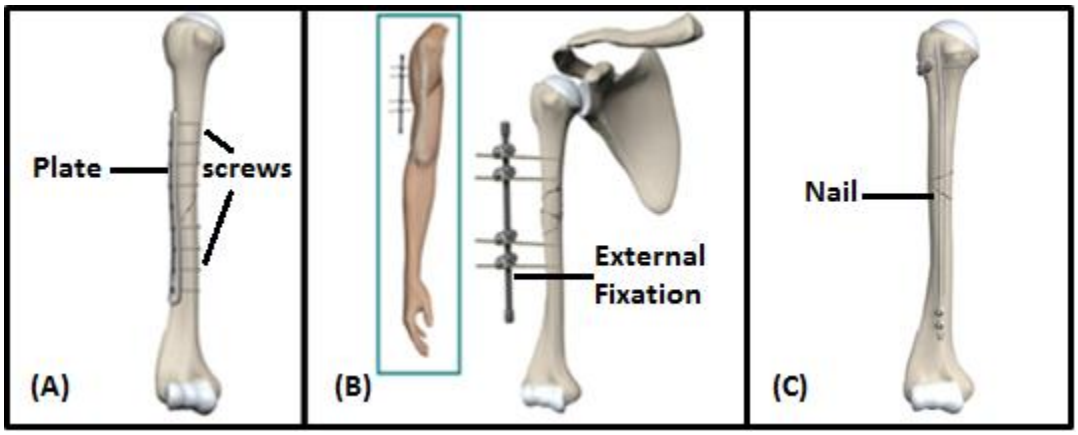

Figure 2.3. Surgical treatments for femur shaft fracture. A) Plate Fixation. B) External Fixation. C) IMN [28].

2.2 The Intramedullary Nailing Technique (IMN)

This section presents the IMN technique and the most popular methods that are used to lock the distal holes. At the end of this section, a summary table shows the comparison between all methods.

Gerhard Kuntscher created IMN treatment method in 1940. Since then, numerous different shapes and designs of IMN are available in the market. The preferred method today for the orthopedic surgeons is the Reamed locked nail as shown in Figure 2.4, [6].

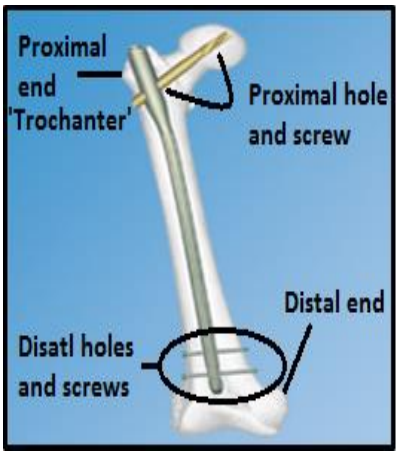

Figure 2.4. Intramedullary Nail [29].

Each surgeon prefers a different patient position for surgery. Commonly, the lateral and supine positions are used to have better access to the trochanter which is the proximal part of the femur. To straighten and align the femoral fracture, traction is applied. A skin incision is then made over the proximal part of the femur. Bone awl and hand reamer are used to penetrate the cortex and medullary canal respectively (Figure 2.5-A and B). After that, an olive-tipped guide wire is inserted into the medullary canal until it reached the distal part of the femur (Figure 2.5-C). By using the reamer over the olive-tipped guide wire, the medullary canal is made wider than the intramedullary nail by 1 mm at least. In Figure 2.5-D and E, external hand force, gentle hammering, and drilling are used to insert the IMN into the medullary canal [6].

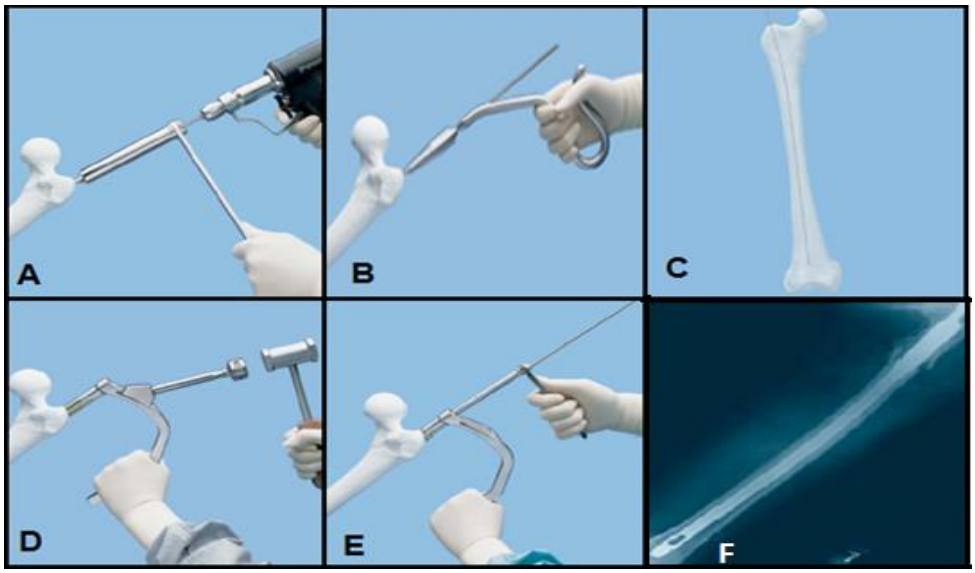

Figure 2.5. Intramedullary Nail process: A and B) Bone awl and hand reamer. C) Olive-tipped guide wire. D and E) Hammering and hand external force to insert the IMN. F) Inserted IMN, lateral X-ray [29].

After the IMN is completely inserted, the process of locking the nail will start (Figure 2.5-F). The insertion of proximal cross-screws is straight forward. It can be achieved via a targeting mechanical guide as illustrated in Figure 2.6.

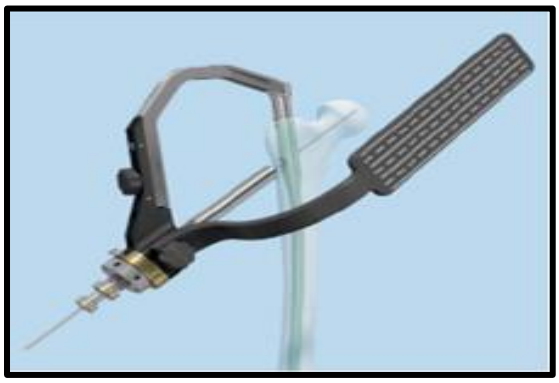

Figure 2.6. Targeting mechanical guide for proximal cross-screw [29].

There are two main reasons that make IMN insertion of distal cross-screws challenging. The first is the insertion of distal cross-screws. When external forces are applied on the IMN it results in nail deformation. The second reason is that the fluoroscopic images are in 2-D while the surgeon needs 3-D images to target a specific drilling path [15, 16, 21]. With this, at least 11 fluoroscopic images are required.

2.3 Distal Hole Locking Techniques

Numerous techniques and devices have been introduced for locating the distal holes for IMN. These include fluoroscopic techniques, magnetic techniques, lighting techniques, self-locking techniques and robot-assisted techniques. This section will explain and compare these different techniques.

2.3.1 Fluoroscopic Techniques

The most popular and preferred method for surgeon to insert distal cross-screws is the free-hand technique [1, 3-9, 11, 13-18].

To obtain perfectly circular holes on the acquired images, the C-arm of the image intensifier can be adjusted perpendicularly to the nail's hole. It does not matter which one of the two holes will be focused to have perfect circle. Any one of them can act as a reference for the second. A sharp-pointed pin is then lined up over the skin at the center of the perfect circle then fluoroscopic images are taken to confirm correct alignment

(Figure 2.7). At that point, a skin incision is made with respect to perfect circle. The sharp-pointed pin is inserted to the surface of the femur bone. It is then depressed with a sharp-pointed pin to prepare the bone for drilling and inserting the screw. For the second distal screw, the same process is followed [6].

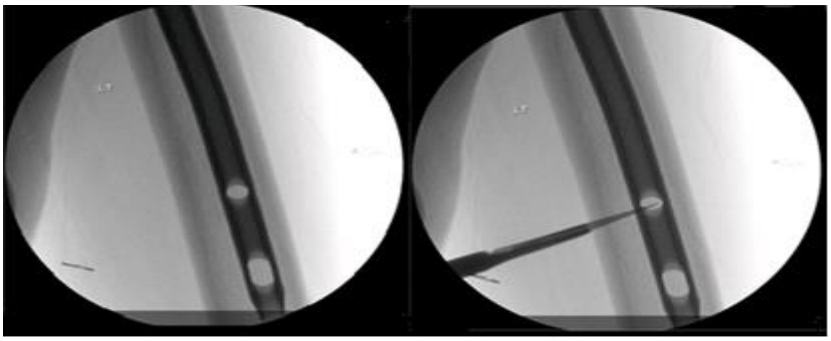

Figure 2.7. Fluoroscopic image showing the distal hole with perfect circle and sharp-pointed pin insertion with respect to distal screw hole [4].

The free-hand technique is time-consuming as the distal locking time is ranging from 15 to 55 min. The ranged number of fluoroscopic images required between 11 to 81 [13]. The time and number of images required for IMN depend on the surgeon's experience. However, it is still an accurate method.

Christos K. Yiannakopoulos et al. in [18] reported another technique in order to decrease the number of fluoroscopic images taken in the free-hand technique. They used two metallic devices to perform distal locking known as *flag and grid*. The metallic grid's dimensions are 20 x 10 cm for all external shape and 10 x 10 mm for internal small quadrant box. This metallic (stainless steel) grid is attached laterally to the skin above the

femur as illustrated in Figure 2.8. Once the IMN is inserted, fluoroscopic images are obtained to detect the perfect circle of distal holes with respect to any grid's quadrant. The hemostatic clamp is attached with the grid to match it with holes (Figure 2.9). The flag device is 20 cm long and is attached with a Steinmann pin, which is sharp and thin to penetrate easily through the skin and into the bone cortex. The surgeon chooses any distal cross-screw hole to start the insertion process. As soon as the distal cross-screw hole is open by the Steinmann pin, the insertion of the distal locking screw can be performed.

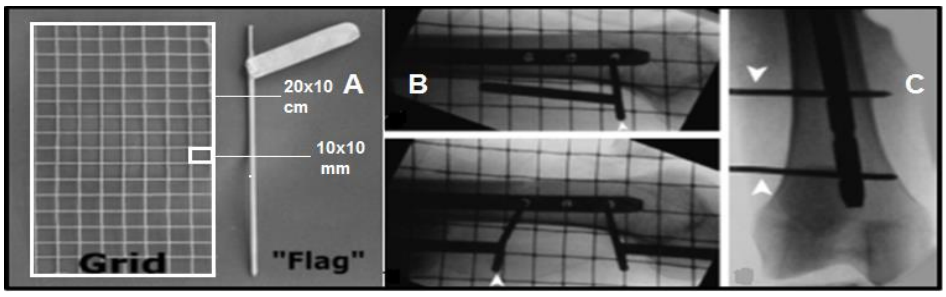

Figure 2.8. Flag and Grid method. A) The Grid and Flag instruments. B) Side fluoroscopic image of the femur viewed with one flag and two flags (arrowhead) centered on the distal holes of the nail. C) The flags passed off the distal nail holes [18].

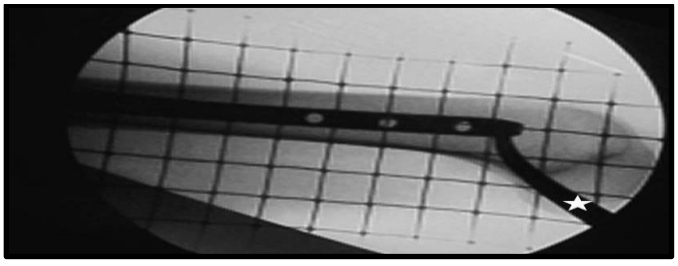

Figure 2.9. Lateral fluoroscopic image showing the relationship between the distal holes of the IMN and the grid. A hemostatic clamp (star) is used to match the grid with holes [18].

The results of the flag and grid technique show that the time for distal locking is between 2.4 to 7.8 min and the number of fluoroscopic images required is between 5 and 9. The technique was successful in all experimental trials (62 cases) but the radiation exposure is relatively high.

George Anastopoulos et al. in [1] designed another technique to decrease the radiation exposure and surgery time. This technique is used in a newly introduced commercial device (Stryker S2™ Intramedullary Nail, Distal Targeting Device).

The new device has a groove between the two distal holes which assists in determining the distal hole (Figure 2.10-A). A beveled-tip probe and a targeting device with three central circular holes are aligned on a perpendicular axis between the two locking holes (Figure 2.10-B). Once the nail is completely inserted into the IM canal, fluoroscopic images are taken to determine the distal nail holes position by using the three circles as reference as shown in Figure 2.11.

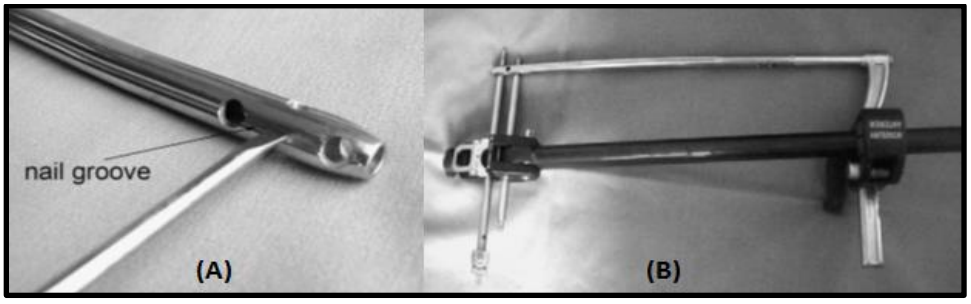

Figure 2.10. Stryker S2™ Intramedullary Nail, Distal Targeting Device. A) Two distal holes with the beveled-tip probe fall in nail groove. B) Assembly of targeting guide device with nail and calibrated from proximal and distal part [1].

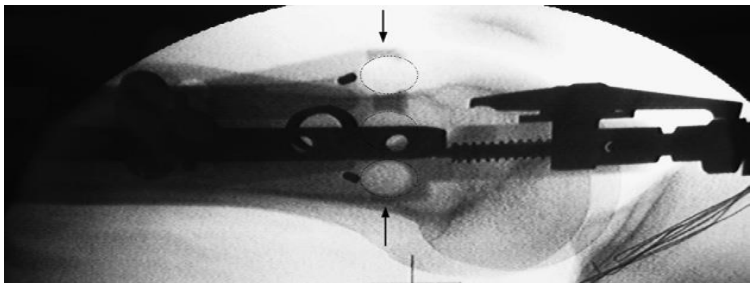

Figure 2.11. Side fluoroscopic image for the targeting device and distal screw nail holes that shows the central circle is closer to distal cross-screw hole and chosen as pilot hole [1].

The duration for distal locking ranged between 4 to 9.2 min. Only two fluoroscopic images were taken in all successful cases. Screw insertion failed in 3.9% of the cases, while 6.1 % developed minor complications.

Rajesh Rohilla et al. in [13] developed the Nail Over Nail (NON) technique where two nails are used. The first nail is inserted into the medullary canal following the standard procedure. The second is connected to the first nail by inserting a trocar and cannula through the hole of the proximal guide and into the proximal part of the second nail (Figure 2.12) parallel to the skin and laterally to the thigh.

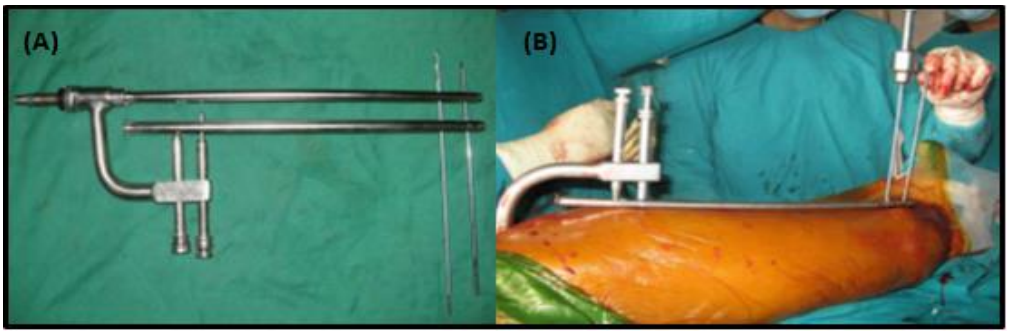

Figure 2.12. Nail over Nail method. A) Assembly of Nail Over Nail parts. B) The technique of locating the distal cross-screws [13].

To avoid nail deformation during insertion, the NON-technique requires 1.5 mm over-reaming (opening the medullary canal prior to insert the intramedullary nail). However, when the insertion of the first nail is complete, fluoroscopic images are needed to determine the exact position of distal holes with comparison to the external nail.

The result for NON-technique shows that there is a chance of missing the location of distal holes. Five screws failed out of 70 cases and 5 were inserted with difficulty in this study. The time of distal locking is between the ranges of 15 to 41 min with relatively high radiation exposure. Fluoroscopic images required are between 1 and 21. Over-reaming the medullary canal and large skin incision is necessary.

2.3.2 Lighting Techniques

William Chu et al. in [5] created another technique for locating the distal holes without fluoroscopic images. This technique depends on a strong light source (LED), which is called intramedullary endo-transilluminating (iMET). The light source consists

of a power source, a catheter and LED. The light at the top of the catheter can penetrate the bone and all barriers and will be visible to the naked eye (Figure 2.13-A). The next step after the IMN insertion is to insert the catheter with LED through it. The length of the catheter should be the same as that of the IMN. The LED should be exactly at the center of the distal hole. Slight adjustments can be made to the catheter until the underlying light can be clearly visible as a clear circle (Figure 2.13-B). Sometimes, the surgeon needs to reduce the light source inside the operation theater to improve the visibility of LED spot light. An incision is made at that location and the hole is drilled. Before the drill reaches the bone cortex, the catheter is removed and the screws are inserted.

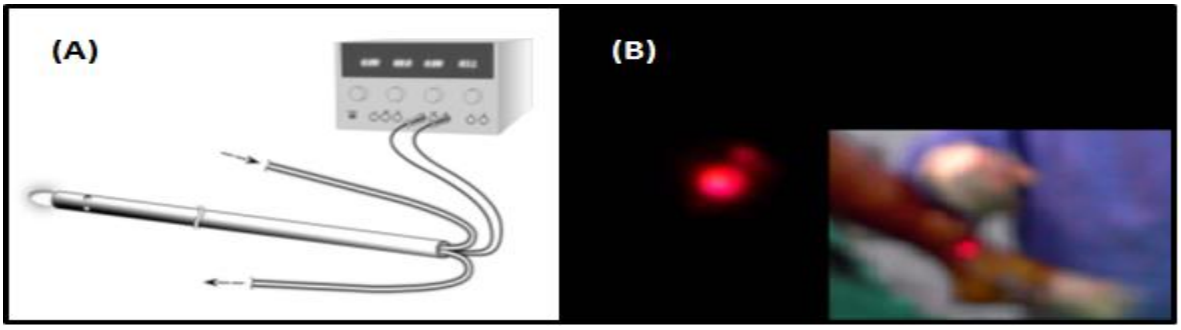

Figure 2.13. Intramedullary endo-transilluminating (iMET). A) Schematic diagram for iMET device with strong light source (LED). B) Surgery theater with dimmed lights. The spot of light from the source appears very clear on the surface of the skin above the tibia bone [5].

In this technique, no fluoroscopic images are taken and no failures were reported. The time required for one distal locking ranged between 2.3 to 5.8 min. Unfortunately,

the researchers did not calculate the time required for catheter insertion. The system was tested on patients with tibia-fracture. However, the anatomy of lower leg bones (Tibia bone) and tissues surrounding is totally different from femur bone and the tissues surrounding. Tibia bone is superficial and very close to the skin while the femur bone is much stronger, heavier, and surrounded by large muscles and thick tissues. Due to high intensity of light used in this technique, thermal burns of the bone have been reported.

2.3.3 Self- Locking Techniques

Guodong Wang et al. in [17] worked on the validation of the new intramedullary propping nailing (IPN or Pan's Nail) which was designed by Professor Pan. This is used to stabilize the femur fracture by means of four longitudinal branches of four spines fitted with ditch grooves located at the distal end of nail. IPN distal hole interlocking is no longer required in this procedure. As illustrated in Figure 2.14 the IPN is inserted inside the IM canal and the inner rod inside the IPN rotates until tight nail-to-bone contact occurs and the four spines in the distal part of IPN open in four directions.

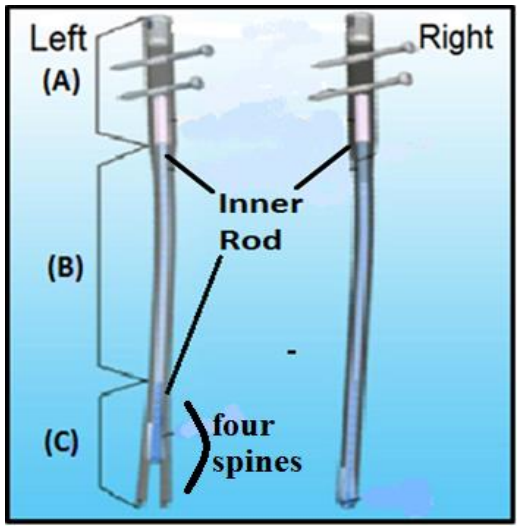

Figure 2.14. Intramedullary propping nailing (IPN), the IPN before propping (right), the IPN after propping (left). A) Proximal part of IPN, operative part. B) IPN body. C) Distal part of IPN, propping part where the four spines allocate [17].

In this study, researchers compared the IPN with Grosse and Kempf (G&K) nails. This G&K nail is a regular nail with a distal lock and is available in the market.

Real femur bones (collected from cadavers) with transverse fractures were used in tests. Three kinds of tests are used: axial compression, four-point bending, and torsional testing see Figure 2.15. All of these tests showed that the IPN is stable and better than regular nails. Fluoroscopic images are not required here. On the other hand, more tests are needed to evaluate post operation fatigue test and the effectiveness of the technique on different types of fractures.

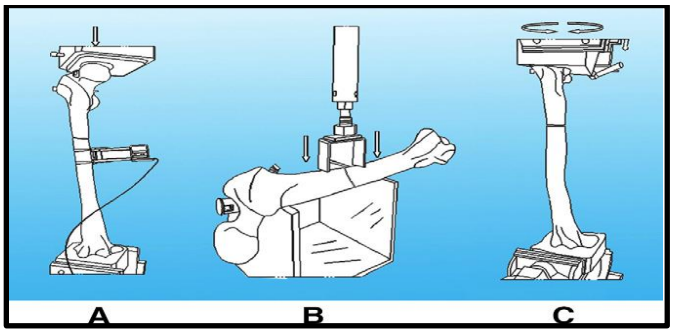

Figure 2.15. Three tests for IPN. A) The axial compressive test. B) Bending test. C) Torsional stiffness test [17].

2.3.4 Robot-Assisted Techniques

In the last few decades, there has been huge progress in using computers, robotics, and surgical robots to achieve better surgical performance.

Z. Y. and L. Joskowicz. in [8] developed a robot-assisted distal locking system. The system consists of a robotic drill guide, an image calibration ring attached to X-ray C-arm (C-Arm is a fluorescence penetrating device that delivers 2-D real-time images), a video frame grabber and a computer. The IMN insertion is done manually as mentioned earlier. At the stage of determining the distal holes, fluoroscopic images are taken to locate the distal holes in comparison to the position of the robot. The position at which the targeting drill will be sent is determined by the computer software. The location is confirmed by inserting a wire in each drill guide. As soon as the location of the distal hole is known, the surgeon starts drilling and continues the operation manually.

In this technique, fluoroscopic images are still required. It was also reported that

some screws were not inserted successfully making the accuracy of the system questionable. Unfortunately, the researchers did not mention anything about the difficulty of the operation or the pre-operation preparation.

M. X. Kong et al. in [9] modified the robot-assisted system. At least two fluoroscopic images are needed to obtain the precise position and orientation of the distal holes. These images are handled by an image-processing software via a computer that converts images to 3-D. The orthopedic surgeon controls the robot manually or remotely. However, it is difficult and risky for surgeons to control the robot without detecting the position of the holes. To solve this, researchers developed a 3-D Model and new algorithms that will warn the surgeon in case of any mistakes or hazards.

This method requires more experiment for validation purposes and surgeons need to be expert in its operation before actually using it. Although there has been a significant decrease in the number of fluoroscopic images with this technique, images are still required to perform the operation of distal locking. Furthermore, the preparation for surgery is very difficult.

Sakol and Jackrit. In [15, 16] proposed another robotic system by using a laser-guided robot and fluoroscopic navigation to determines the position and orientation of distal holes. This helps the surgeon in drilling for distal holes while concentrating on the surgical incision site without monitoring the display graphic information in the same time. After capturing fluoroscopic images which are in 2-D and converted to 3-D by an Image Processing Unit (IPU), the orientation, the position and the coordinates of distal

holes become known. The coordinates are sent to the guidance system of the robot to generate a navigation trajectory path. At this point, a laser beam guides the surgeon to drill. The system interacts with the surgeon to send information and receive a command without reducing hand-eye coordination. On the other hand, the radiation exposure is still present in spite of decreasing the number of required images. Currently, there are no patient statistics available for validation.

2.3.5 Magnetic Techniques

A group of researchers in [23] made a comparison between an electromagnetic navigational and the free-hand technique in terms of time consumption, accuracy, and radiation exposure. The electromagnetic navigational is known in the market as *SureShot; Smith & Nephew* as shown in Figure 2.16.

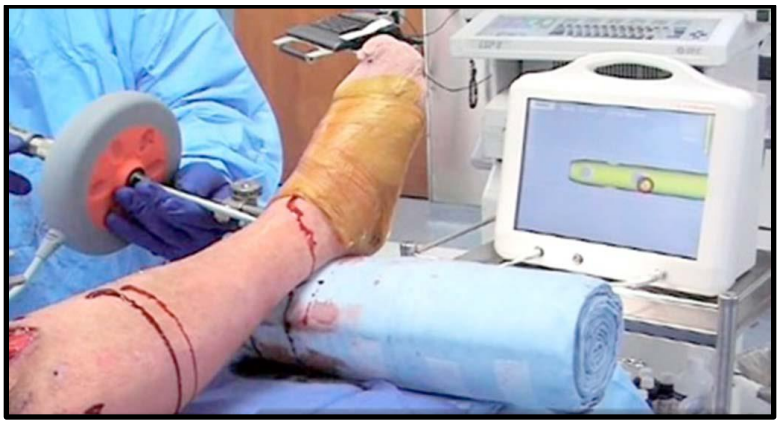

Figure 2.16. Electromagnetic navigational device in real tibia fracture operation [23].

The results show zero error for both techniques for IMN insertion. On the other hand the mean number of fluoroscopic images for distal locking in free-hand technique is 32.9. For electromagnetic technique, no fluoroscopic images have been used. It was noted that the set-up for free-hand technique is faster to do. While hole location and insertion is faster to detect in the electromagnetic technique. In spite of the good results achieved in this study, not all cases are chosen randomly. The majority of the cases tested using the electromagnetic method are Tibia fractures while free-hand technique is used for femur fractures. As described earlier, IMN operations for femur fractures are more challenging. It requires that the operation instruments should be non-magnetic metal to prevent distortion of the electromagnetic signal.

2.4 Comparison of Distal Locking Techniques

Different distal locking techniques were reviewed with respect to radiation exposures, distal locking time, advantages and disadvantages. Table 2 summarizes all the above-mentioned attributes of each technique.

Table 2: Comparison between all the different distal locking techniques

Techniques	Exposures in distal locking *(range)*	Distal locking time *(mean in min/range)*	Advantages	Disadvantages
Fluoroscopic				
Free hand [4, 6, 13]	11 to 81 fluoroscopic images	The range is (15-55) min.	- Easy to master. - No need for an expert surgeon.	- Ionizing radiation is high. - Multi-drilling. - Time-consuming.
Flag and Grid [18]	5 to 9 fluoroscopic images	The range is (2.41-7.8) min.	- The errors are rare. - Easy to master. - Flexible. -Inexpensive.	- Ionizing radiation still relatively high. - All tests are only done for Tibia fracture, no guarantee for the result if tested in fractured femur.
Stryker S2™ Intramedullary Nail [1]	2 fluoroscopic images at least (required).	The mean is 6.6, the range is (4-9) min and 2.6 STD.	- Required radiation is reduced. - Time is reduced.	- Ionizing radiation still required. - Not accurate (3.9% missed distal locking). - 6.1 % of distal locking with minor complications. - Needs expert surgeon.
Nail Over Nail [13]	1 to 21 fluoroscopic images	The mean is 24.34, the range is (15–41) min and 6.04 STD.	- The surgeon can use it if no intensifier images are available.	- Ionizing radiation still relatively high. - Not accurate. - Over-reaming the medullary canal of the bone. - Large skin incision made.
Lighting				
Intramedullary endo-transilluminating (iMET) [5]	No fluoroscopic images.	The range is (4.1 ± 1.8) min.	- No radiation. - Accurate with zero error.	- Not tested for femur fracture. - The time of catheter insertion is not calculated. - It can cause thermal burns to the bone.
Self-Locking				
Intramedullary propping nailing (IPN) [17]	No fluoroscopic images required.	Not yet implemented.	- Stable, comparable or better than regular IMN for femur transverse fracture.	- Not tested in other femur fracture type experiments. - Need more tests like fatigue test.
Robot-Assisted				
Surgical robots, robot-assisted distal locking [8, 9, 15, 16]	At least two fluoroscopic images required.	Not mentioned.	- Reduce the radiation exposure.	- Does not eliminate exposure to radiation. - The robots are expensive and not available in all operation theaters. - Need more measurements for validations.
Magnetic				
Electromagnetic navigational [23]	No fluoroscopic images required.	8.6 minute.	- No radiation. - Accurate (with zero error).	- Need different metal equipment. - Not used for all cases. - The majority of cases were applied on tibia fracture.

2.5 Chapter Summary

The IMN technique is widely used by the majority of orthopedic surgeons in the treatment of long bone fractures. The procedure requires insertion of IMN through the canal of the fractured bone and is fixed at the proximal and distal parts. The locking process is different between proximal and distal parts. For proximal locking, a targeting mechanical guide is utilized and it is a straightforward procedure. For distal locking, the work is challenging due to nail deformation during the insertion process.

Numerous techniques and devices have been introduced for locating distal locking. These include fluoroscopic (free-hand technique), magnetic, lighting, self-locking, and robot-assisted techniques. Fluoroscopic techniques are easy to master, inexpensive, and available in all hospitals, however, they employ x-ray imaging (ionizing radiation). The robot-assisted techniques are expensive and not available in all operation theaters but the radiation exposure is much lower than fluoroscopic techniques. For example in the free-hand technique, the number of fluoroscopic images required for distal locking is between 11 to 81 while in robot-assisted techniques, the number of fluoroscopic images required is 2 to 10 only. In magnetic, self-locking and lighting techniques, no fluoroscopic images are required but these methods either have not been tested for femur fractures or have not been tested for all types of femur fractures. More validation experiments are required.

Currently, an optimal solution for distal locking does not exist. Despite the radiation risks, most of the surgeons still prefer the oldest method which is the free-hand technique. They find it easy to perform, not complicated and available in all hospitals.

3 NUCLEAR MAGNETIC RESONANCE AND MAGNETIC RESONANCE IMAGING

This chapter provides an introduction to the Nuclear Magnetic Resonance (NMR) phenomenon, and Magnetic Resonance Imaging (MRI).

3.1 Introduction to NMR

In MRI, the images are formed by signals acquired from protons (hydrogen nuclei) in water. By nature, each nucleus is spinning rotationally around its axis. This action will create a magnetic moment μ, and so can be assumed as a tiny bar magnet with two poles, south and north in a direction along the spinning axis as shown in Figure 3.1-left. Furthermore, μ has a fixed magnitude and the alignment is completely random. In case that there is no influence from an external uniform *magnetic field* B_o on the protons (hydrogen nuclei), the net magnetization for all protons is zero as shown in Figure 3.1-right, [30, 31].

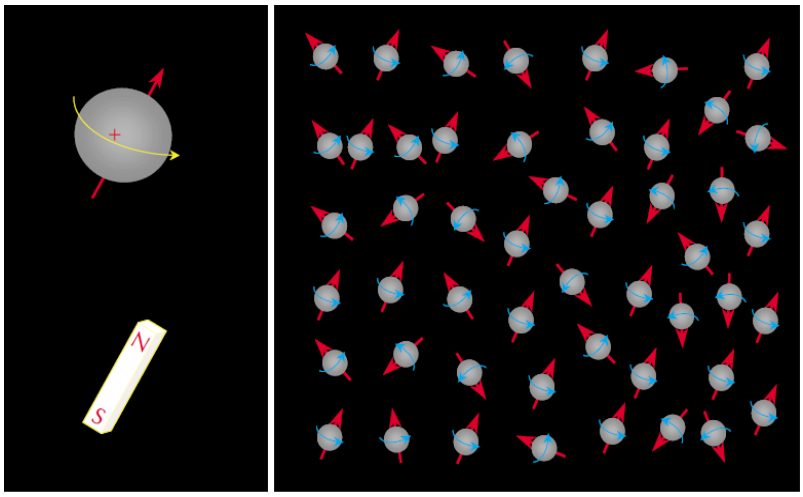

Figure 3.1. Hydrogen nucleus acts like small bar magnets (left). The magnetic moments in random directions, lead to their cancellation (right) [32].

There are three stages in NMR as listed below:

- *Polarizing stage.* In this stage, a bulk magnetization is generated when uniform external B_o is applied.
- *Excitation stage.* Starts when a Radio Frequency RF pulse is applied to rotate the net magnetization.
- *Detection stage.* Starts when the RF is turned off and spins are precessing freely.

In the polarizing stage, once the protons are exposed to an external uniform B_o, the nuclear spin will align either parallel (up with low energy) or anti-parallel (down with high energy) along the direction of the external B_o. However, this alignment is not perfect see Figure 3.2, [33].

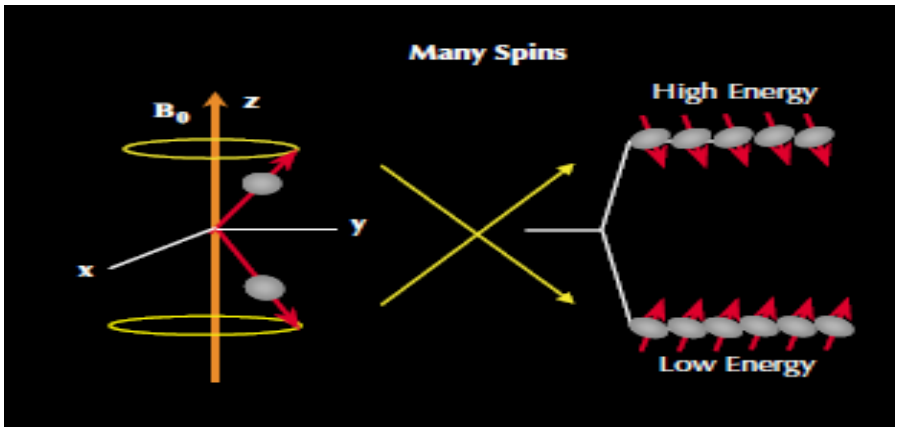

Figure 3.2. The nuclear spin aligns either parallel or anti-parallel along the direction of Bo [32].

Each spin direction for parallel or anti-parallel possesses a magnetic energy given by Eq (1).

$$E_{\mu} = -\gamma \hbar \mu B_o \qquad (1)$$

where:

- γ is a gyromagnetic ratio, which is a constant for any particular type of nucleus. For Hydrogen ^1H this is 2.675×10^8 $s^{-1}T^{-1}$.
- $\hbar$ is Plank's constant $\frac{6.63 \times 10^{-34}}{2\pi}$ Js.

Due to thermal motion of the nuclei of molecules, and the interaction between the nuclear spins in terms of energy exchange, there is a very small population difference between the lower energy (spin up) and higher energy (spin down) nuclei. The relation is shown in Eq (2).

$$\frac{N(higher)}{N(lower)} = \exp^{-\gamma Bo/kT} \qquad (2)$$

where:

- N is the number of nuclei to spin either up or down.
- K is the Boltzmann constant.
- T is the temperature in Kelvin.

Although the difference is small, it is enough to generate a bulk magnetization component aligned longitudinally with the uniform external B_o and the Z direction. The B_o direction is always along the Z-axis. On the other hand, the transverse (X, Y) plane components tend to cancel each other (Figure 3.3).

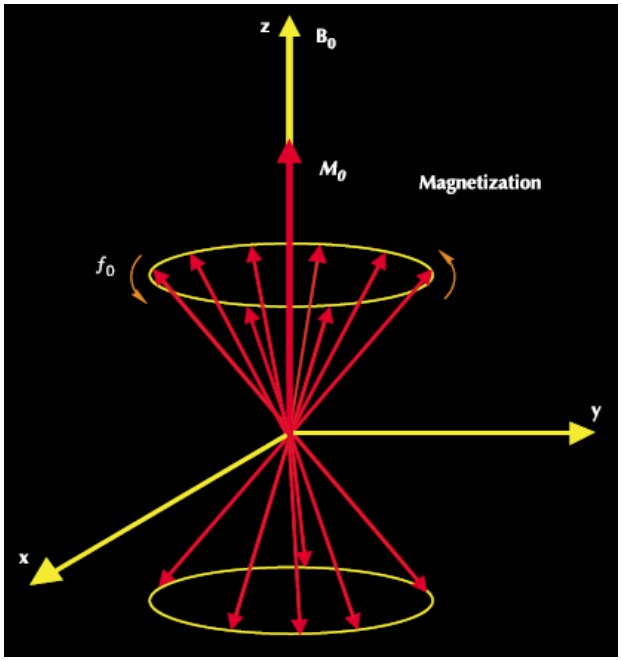

Figure 3.3. The net magnetic component with Z-axis and along the direction of Bo [32].

The protons will precess around B_o with a frequency directly proportional to its strength. This frequency is called the Larmor frequency. The relationship between Larmor frequency and B_o is given by Eq (3).

$$\omega = \gamma B_o \qquad (3)$$

In EFNMR, there are two external uniform B_o: 1) the first is present during the application of a polarization pulse in the polarization stage and it donates B_p, 2) the second is the Earth's magnetic field and is present after switching off the polarization pulse. It is donated by B_E. The excitation and detection stages happen during B_E.

During the polarization stage, the net magnetization component will be generated. When B_p is switched off the net magnetization will rotate along B_E. In the excitation stage of MRI, a short Radio-Frequency (RF) pulse is applied. For example, an RF pulse applied about the Y-axis will cause the net magnetization to rotate about the X-axis from the Z-axis or vice versa. If the RF pulse is applied about the X-axis, the net magnetization will rotate about the Y-axis from the Z-axis. The net magnetization rotation depends on the duration and strength of the applied RF pulse. This rotation angle of net magnetization is defined by the *tip angle* θ as shown in Figure 3.4, [34].

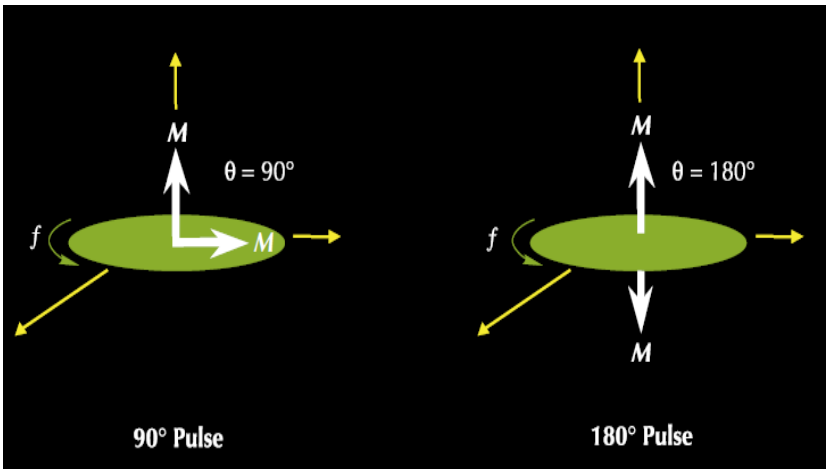

Figure 3.4. The magnetic vector rotates to transverse (x, y) plane after application of 90° RF pulse (left). The magnetic vector rotates from Z positive to Z negative after application of 180° RF pulse (right) [32].

In the detection stage, the RF pulse is turned off and the excited spins work to recover their orientation and equilibrium energy. This is illustrated in Figure 3.5 and called Free Induction Decay (FID).

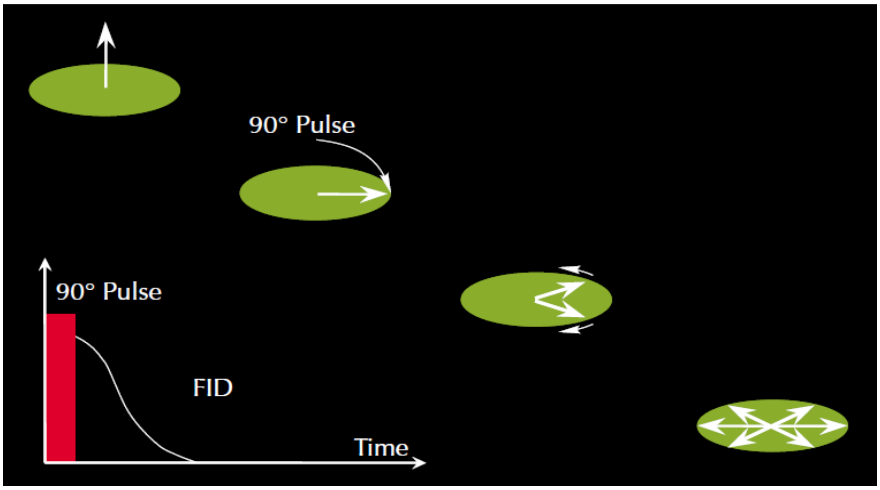

Figure 3.5. The FID signal detected after application of RF pulse [32].

3.2 Spin-Echoes

After a 90° RF pulse is applied, the NMR signal appears as the spins are precessing in-phase in the transverse plane. Two factors that affect the spins precessing in-phase are *spin-spin relaxation* which is irreversible and the *magnetic field inhomogeneity* which is reversible by using a Spin-Echo sequence. Therefore, the spin-echo helps to fix the de-phasing that happens due to magnetic field inhomogeneity by applying a 180° RF pulse after a 90° RF pulse. The time between the maximum echo after the 180° RF pulse is equal to the time between the two pulses and this is called *echo time* τ_E as shown in

Figure 3.6. Therefore, the signal will be detected and sampled after two τ_E [33, 35].

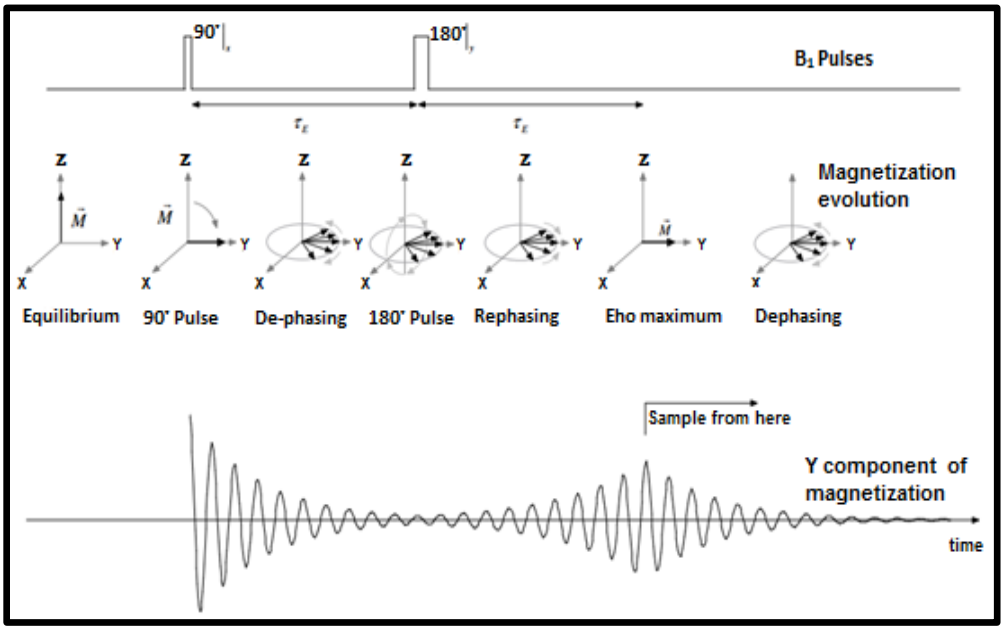

Figure 3.6. Spin echo sequences [33].

The echo time should be accurate to have a NMR signal. In Figure 3.7, another view of the spin-echo sequence is illustrated. There are five stages for the spin-echo sequence:

- Stage 1. The 90° RF pulse is applied.
- Stage 2. The de-phasing is in progress.
- Stage 3. The 180° RF pulse is applied after τ_E.
- Stage 4. The re-phasing proceeds.
- Stage 5. The echo of FID signal is at maximum and this happens after two τ_E.

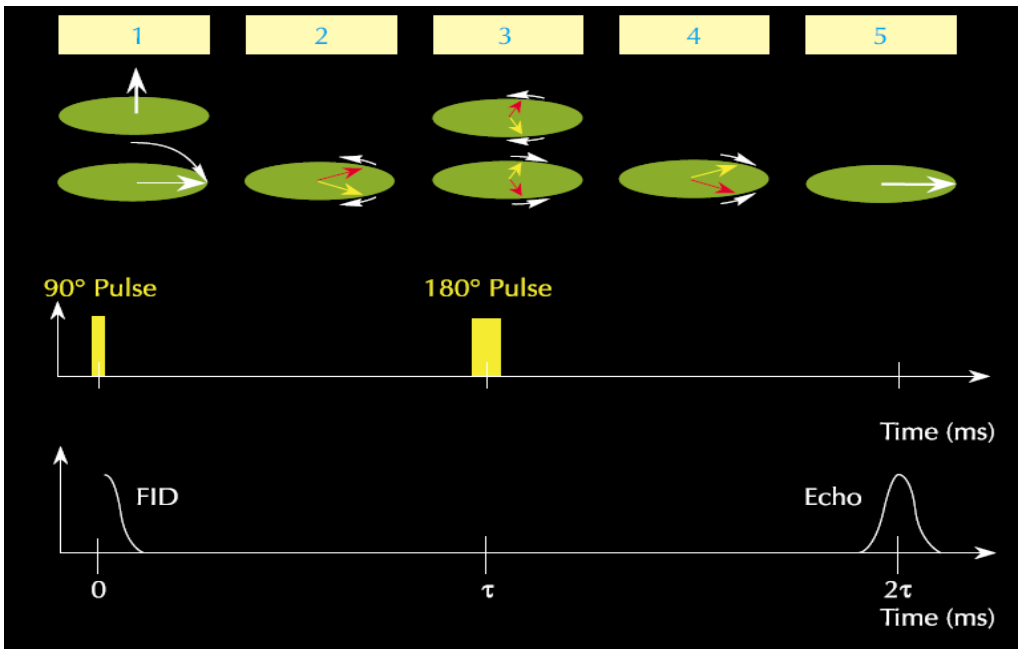

Figure 3.7. shows the spin-echo stages [32].

3.3 Relaxation

The magnetic moment vector that is aligned with B_E is called the longitudinal magnetization. In the excitation stage when the RF pulse is applied at the Larmor frequency, the magnetic moment vector will rotate around the transverse plane perpendicular to the Z-axis and the energy equilibrium of the system will be disturbed. After the excitation stage, the spins take time to recover their orientation and equilibrium energy. This time is called relaxation. There are two processes associated with relaxation these are explained in the following subsections.

3.3.1 Spin-Spin (Transverse) Relaxation: T_2

The NMR signal that arises depends on two factors: 1) the spin-spin relaxation process which is represented by the relaxation time constant T_2, and 2) the homogeneity of the static B_o which is represented by the relaxation time constant T_2*.

When a 90° RF pulse is applied, the magnetic moment will precess in-phase in the transverse (X, Y) plane. In cases where the static magnetic field's inhomogeneity leads to spins precessing out of phase, the transverse relaxation time will be faster and the FID signal will be shorter. Thus, T_2* is shorter than T_2. In case where the static magnetic field is homogeneous, the FID signal will depend on relationship between the two pairs of nuclei. Each nucleus has a small magnetic dipole moment. It is called local magnetic. This affects the precessing of each nucleus by moment dipole-dipole interaction between

two neighboring spins. This interaction is known as spin-spin relaxation.[33-35].

To measure T_2 more accurately, the spin-echo will be used to refocus the de-phasing of the magnetization produced by the inhomogeneous field.

3.3.2 Spin-Lattice (Longitudinal) Relaxation: T_1

T_1 is the time constant of the longitudinal magnetization component in order for the nuclei to return back to their orientation (Z-axis) and equilibrium energy. When the nucleus spins in the transverse plane after excitation, the excited nucleus will start to release its energy to the surrounding lattice. This is called longitudinal relaxation or spin-lattice time, T_1. As shown in Figure 3.8 there are two different longitudinal relaxation times in EFNMR:

1. The Polarizing Pulse field (B_p) time.
2. The Earth's Magnetic Field (B_E) time.

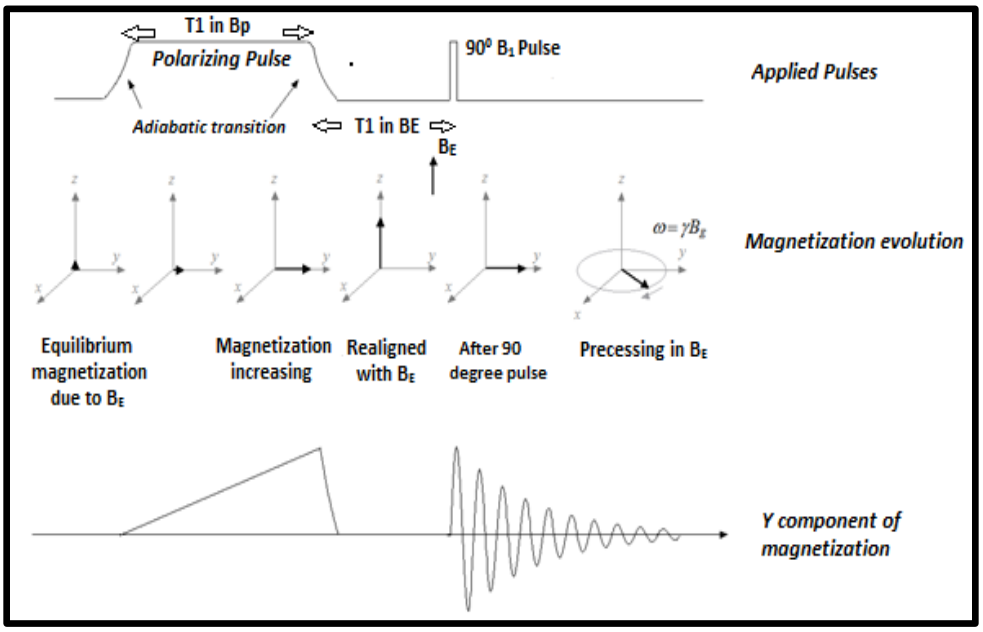

Figure 3.8. The sequence diagram showing the polarizing pulse (Bp) with increasing magnetization vector and realigning of the vector with Earth's magnetic Field (BE) after stopping the polarizing pulse [33].

3.4 Carr-Purcell-Meiboom-Gill (CPMG) Pulse Sequences

As descried earlier, there are two factors affecting the de-phasing of NMR signal: first, spin-spin relaxation which is irreversible; second, magnetic field inhomogeneity which is temporarily solved by spin-echo after the application of 180° RF pulse.

The Carr-Purcell-Meiboom-Gill (CPMG) pulse sequences start with a 90° RF pulse followed by multiple 180° RF pulses to keep fixing the spins de-phasing related to field inhomogeneity. The time period between the 180° RF pulses is twice the time between the 90° RF pulse and the first 180° RF pulse. Basically, the start of CPMG pulses is exactly as the spin-echo pulse sequence with a train of 180° RF pulses. This is utilized

to measure the T_2 more accurately than the spin-echo pulse as this method corrects the de-phasing that happens with each single 180^o RF pulse (Figure 3.9).

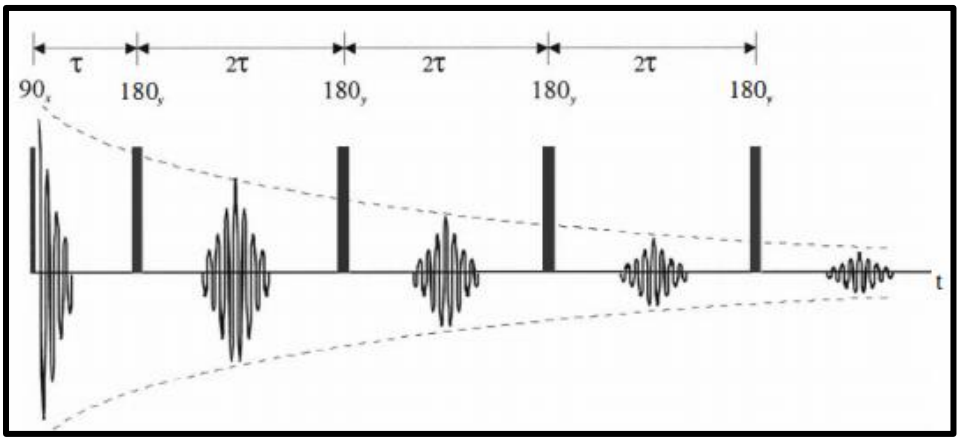

Figure 3.9. T2 decay envelopes with CPMG pulse sequences [34].

3.5 Introduction to MRI

Magnetic Resonance Imaging (MRI) is basically an imaging technique based on the NMR phenomenon. It explores the encoded information in the form of signals through the position of the spins. Theoretically, all spins are exposed to the same strength of magnetic field. But through the use of magnetic gradient fields known as *read gradient*, this will expose the spins to different strengths of magnetic field. Consequently, the spins will be precessing at different Larmor frequencies based on their position. This is often referred to as *frequency encoding*. By using another gradient called *phase gradient*, the spins will acquire a phase offset directly correlated to position. This is often

referred to as *phase encoding*. To produce a one-dimensional image, it is enough to use the read gradient whereas to have two-dimensional images, both read and phase gradients will be needed. In the following subsections, the MRI pulse sequences *gradient-echo imaging* and *Spin-echo imaging* will be described.

3.5.1 Gradient-Echo Imaging

The *gradient-echo imaging* pulse sequence for MRI experiments is shown in Figure 3.10.

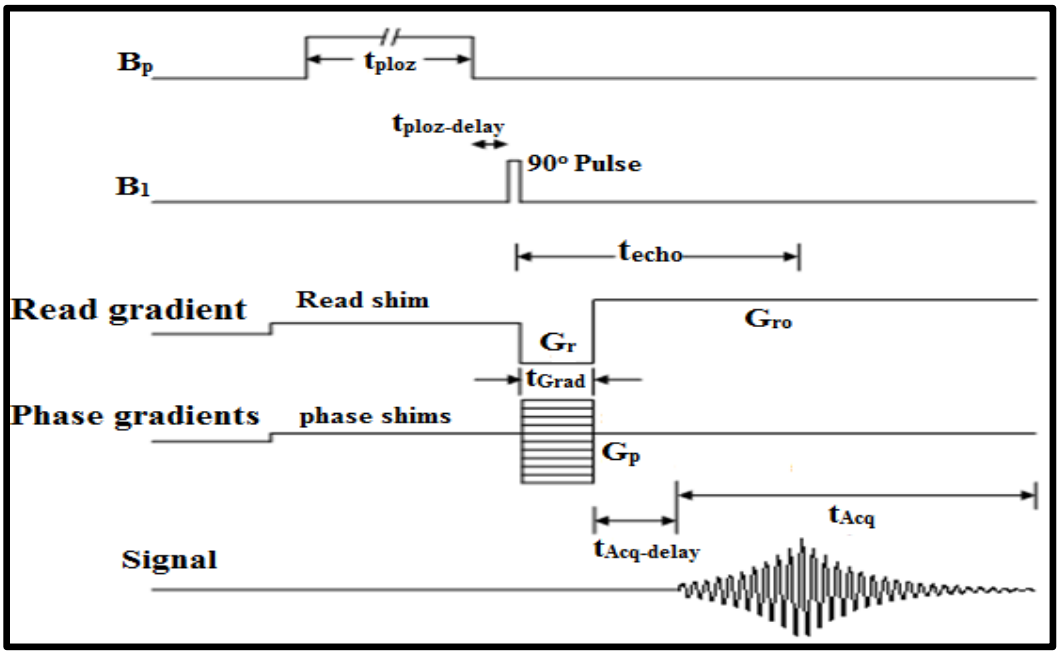

Figure 3.10. Gradient-echo imaging pulse sequences [33].

The below points describe the main parts of the sequence.

- The role of the polarization pulse and 90^o RF pulse (excitation pulse) were described earlier in this chapter. Between the polarization and excitation pulses, there is a short time delay ($t_{ploz\text{-}delay}$ = 50 ms) which allows the current to turn off and the net magnetization to rotate adiabatically until it aligns with the Earth's magnetic field direction.
- G_r and G_{ro} are read gradient and read out gradient respectively. Changing the read gradient exposes each localized group of spins to a different magnetic field strength. Theoretically, $G_r = G_{ro}$ and their addition is equal to the echo time.
- Time gradient expressed as t_{Grad}, is the time from excitation pulse till the gradient change.
- The image is being captured after an echo time.
- Acquisition delay time, $t_{Acq\text{-}delay}$, is the time starting from the gradient change till the beginning of acquisition time which is 20 ms to avoid any B_1 coil ring-down.
- Phase Gradient is the work to shift the phase before capturing the data from the signal.

For 1-D experiments, there is no activation for *phase gradients*, whereas for 2-D a single phase gradient is activated.

3.5.2 Spin-Echo Imaging

The *Spin-echo imaging* pulse sequence for MRI experiments is shown at below Figure 3.11.

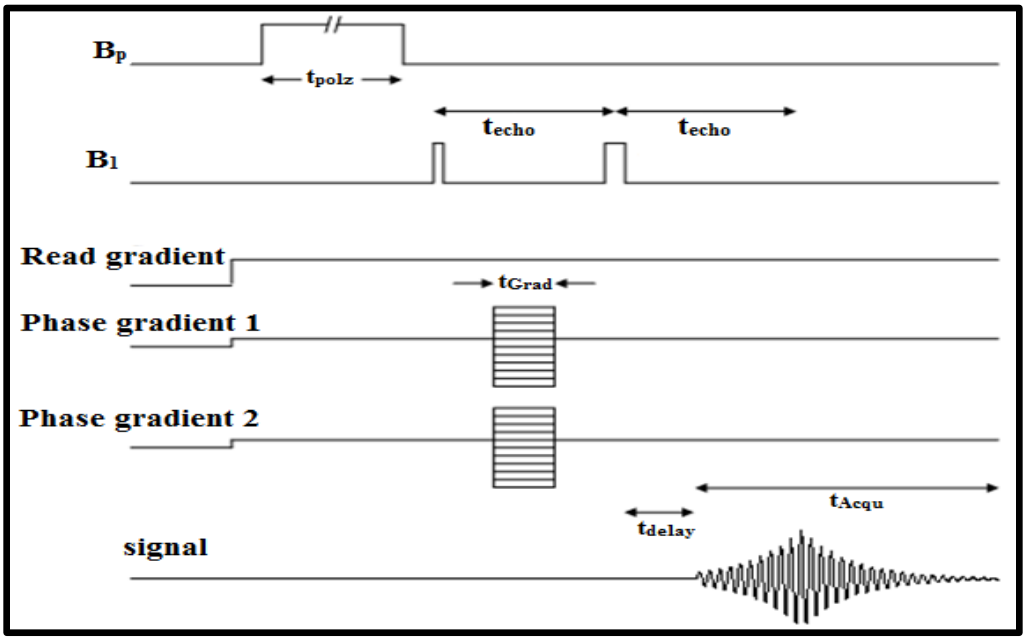

Figure 3.11. Spin-echo imaging pulse sequences [33].

Most of the processes for Spin-Echo imaging are exactly like Gradient-Echo imaging pulse sequence with few differences as listed below:

- The B_1 coil deployed two RF pulses 90^o, then 180^o. Therefore, the spin-echo helps to fix the de-phasing that happens related to magnetic field inhomogeneity.
- The read gradient is activated before RF 90^o pulse and polarization pulse.
- The image is captured after two echo times.

For 1-D experiment, there is no activation for phase gradients. Whereas, for 2-D images, a single phase gradient 1 is activated. The second phase gradient is activated in 3-D images.

Another MRI pulse sequence is available just for 2-D which is called *Filtered Back Projection*. It is used particularly in a few 2-D experiments in this thesis. This method uses data processing and a different reconstruction imaging algorithm. Also the image resolution is better compared to other sequences. On the other hand, data collection is achieved as before and the image is captured after two echo times. For further details regarding this method, the reader is referred to [33, 35].

3.6 Chapter Summary

There are three stages in EFNMR: polarization, excitation, and detection. A pulse is switched on in the polarization stage to produce a bulk magnetization. Once switched off, the bulk magnetization will rotate along the Earth's magnetic field. In the excitation stage, a short Radio Frequency (RF) pulse is applied causing the bulk magnetization to rotate around the transverse plane perpendicular to the Earth's magnetic field. The bulk magnetization rotation depends on the duration and strength of the applied RF pulse. In the detection stage, the RF pulse is turned off and the excited spins work to recover their orientation which is called Free Induction Decay (FID). After the excitation stage, the spins take time to recover their orientation. This time is called Relaxation Time. There

are two processes associated with relaxation time. These are Spin-Spin (Transverse) Relaxation: T_2, and Spin-Lattice (Longitudinal) Relaxation: T_1.

MRI explores the encoded information in the form of signals through the position of the spins. Theoretically, all spins are exposed to the same strength of magnetic field. By using two additional magnetic gradient fields known as read and phase gradient (referred to as frequency encoding and phase encoding respectively), the read gradient field will expose the spins to different strengths of magnetic field. Consequently, the spins will be precessing at different Larmor frequencies based on their position. In the phase gradient field, the spins will acquire a phase offset directly correlated to their position.

The following chapter will show the main parts of the EFNMR apparatus and the detailed description of the most important parameters in the NMR and MRI experiments. The setup of the instrument and necessary precautions will also be explained.

4 EARTH'S FIELD NUCLEAR MAGNETIC RESONANCE APPARATUS

The Earth's Field Nuclear Magnetic Resonance (EFNMR) apparatus or Terranova-MRI was invented in the 1950s by Magritek Limited [36] to serve as a teaching model for NMR and has been used little in research.

Nowadays, the EFNMR apparatus is less expensive, small, portable, and with enhanced features like Carr-Purcell-Meiboom-Gill (CBMG) and multi-dimensional imaging. Hence, both research and education have utilized it more.

4.1 Main Parts of the EFNMR Apparatus

The EFNMR apparatus shown in Figure 4.1 was used for all experiments in this thesis. It has three main parts:

- A three-coil probe.
- A spectrometer.
- A Prospa software.

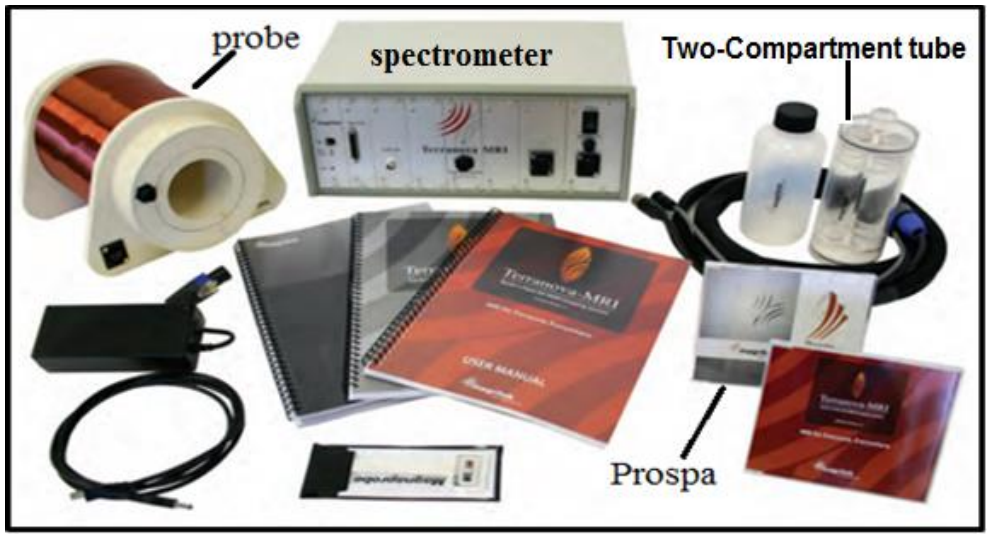

Figure 4.1. Full equipment set, two-compartment tube is used in many experiments [33].

4.1.1 Terranova-MRI Three-coil Probe

The Probe consists of three slots (Figure 4.2). The outermost is called the polarizing coil which is responsible for the initial polarizing field. The middle is the gradient coil which provides a linearly varying magnetic field on the object, and the innermost is called B_1 which is for signal excitation and detection.

Figure 4.2. Three coils Probe [33].

The Polarizing Coil is a large solenoid coil. It provides a calculated magnetic field of 3.13 mT per ampere (A). In case 6 A (maximum value) is applied, the magnetic field will be 18.78 mT. This magnetization will enhance the nuclear magnetization on the object inside the probe. The object in this project is tap water.

The B_1 coil transmits excitation RF pulses and receives the signal back from the object. It is a solenoid coil connected with the spectrometer, which forms a parallel LCR circuit where the inductance (L) and the resistance (R) are fixed values with 0.5 H and 225 Ω respectively. The capacitance (C) is variable between 4.4 and 17.15 nF. The EFNMR signals occur at resonance by changing the value of C. The resonance frequency ω_o is given by Eq (4).

$$\omega_o = \frac{1}{\sqrt{LC}} \qquad (4)$$

When the B_1excitation pulse is transmitted, the B_1 coil resonates and decays over time. This is called the *coil ring-down*. An acquisition delay is applied between the excitation pulse and the first NMR signal point collected to avoid capturing the coil ring-down signal. The gradient coil consists of four gradients Z, Y, and two X. It provides a linearly varying magnetic field on the object by changing the total magnetic field applied on the object.

4.1.2 Terranova-MRI Spectrometer

The pulse sequences are executed and controlled by means of tuning the coils to process the FID signal. A Universal Serial Port (USP) connects the spectrometer with a PC on which the Prospa software is installed. All commands and changes to the experimental parameters are sent via the USP from the Prospa software to a digital signal processing (DSP) unit in the spectrometer. Therefore, more flexibility is achieved in changing and controlling the experimental parameters.

4.1.3 Terranova-MRI Software Package: Prospa

Table 3 lists the typical experimental parameters used both for NMR and MRI experiments using the Terranova-MRI instrument. These parameters can be manipulated through Prospa in three stages: polarization stage, excitation stage, and detection stage. The values in the table are based on values for Qatar only. For other regions, these values could differ depending on the Earth's poles and equator since the Earth's magnetic field is the largest at the poles and decreases towards the equator.

Table 3: Detailed description of the parameters in the experiments.

Parameters and Stages	Parameters Description	Experimental Value Range
Polarizing Currents ***(on polarization stage)***	During the first stage, the current passes through the polarization coil to create a magnetic field. The available maximum value is 6 A to avoid any risk of overheating of Probe and sample. When the current increases, the bulk nuclear magnetization increase also.	4 to 6 A
Polarizing duration ***(on polarization stage)***	This is the time of application of the current in the polarizing coil to maximize the bulk nuclear magnetization. Repeating and increasing the polarizing time with high current will overheat the probe and sample.	400 to 5000 ms
B1 Frequency ***(on excitation stage)***	To rotate the bulk magnetization vector to the transverse plane.	1650 to 1750 Hz
Capacitance ***(on excitation stage)***	A value to tune the B_1 coil and spectrometer in Larmor frequency in the sample and to get a high-quality NMR signal.	16 to 18 nF
Transmit (B_1) gain ***(on excitation stage)***	Controls the amplitude of the excitation pulse which affects the tip angle between the transverse plane and the bulk magnetization. The relationship between gain and tip angle is linear.	0.8 to 3
Pulse duration ***(on excitation stage)***	Controls the length of the excitation pulse which affects the tip angle between the transverse plane and the bulk magnetization.	1.5 to 2 ms
90^o pulse duration ***(on excitation stage)***	The length time of a 90^o pulse that will help to maximize the SNR.	1 to 1.7 ms
180^o pulse duration ***(on excitation stage)***	The length time of a180^o pulse in echo-spin.	2.1 to 2.85 ms
Receive gain ***(on detection stage)***	Controls the amplification of the NMR signal and the noise but does not improve the SNR.	1.5 to 3
Number data points ***(on detection stage)***	The induced signal is sampled and recorded.	1024-384 points
Acquisition delay ***(on detection stage)***	Starts sampling of the induced signal and prevents capturing the coil ring-down decay.	25 ms
Acquisition time ***(on detection stage)***	Data recorded measured in µV and sampled as a function of time	1 to 2 s
Repetition time	The time take to start the next experiment	1.5 to 10 s
Number of scans	The number of times the experiments are repeated. As the number of scans increases the SNR will increases.	Recommended to be more than 3 scans
Average	The average exists if there is more than one scan in terms of improved SNR.	----------

Table 4 shows the experimental parameters for image parameters and pulse sequence parameters, the description and limit value for each one.

Table 4: The MRI experimental parameters.

Gradient – Echo Imaging Parameters	Parameter	Description	Limit
Image Parameters	Dimension	Choose the dimension.	1,2,3
	Orientation	Determine read dimension	X,Y,Z
	Matrix Size	The number of pixels in the image. As the matrix size is increased, the resolution becomes better but it will compromise experiment time.	1 to 512
	Field of View (FOV)	This option with matrix size will affect the image resolution. It is preferred that the FOV size will cover the object. If the FOV decreases, the object will appear larger	0 to 500 mm
Pulse Sequence Parameters	Phase gradient duration	After a time (t_{Grad}), the gradient will change to positive polarity in terms of re-phasing the de-phasing spins. The stage where the spins re-phase is called a gradient echo.	0 to 500 ms
	Echo time	The time between excitation 90° pulse and the center of echo.	10-1000 ms
	Bandwidth	The frequency of collected data across the image.	1-200 Hz

4.2 The Three-coil Probe Direction

In MRI, the position of the object is important. By default, the Z-axis is always with the B_E direction which is the same for the red arrow direction in the probe. The X

direction is along the coil axis and the Y-axis is perpendicular to both axes (Figure 4.3).

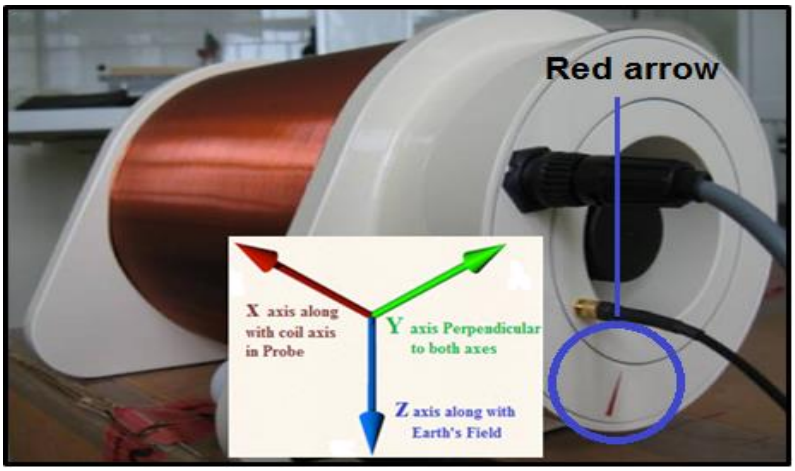

Figure 4.3. Shows the direction of three axes in 1, 2 and 3-D.

4.3 Instrument Setup and Precautions

To avoid any discrepancies in the experimental results, all experiments have been completed with respect to the below points:

- The experimental parameters are adjusted based on the large volume of tap water sample which is almost 500 ml.
- The location of the experiment is very important to be able to execute the experimental procedures and to have an exponentially FID signal. The experiments have been implemented in the same place with noise level ranging between 2.3 to 2.5 μV rms.

- It is recommended to keep away all ferrous or metal objects around the EFNMR apparatus, at least 2 meters away.
- Use a wooden structure as a stand for the probe (Figure 4.4-A).
- The probe should be placed in the center of the room away from the wall and away from any source of low-frequency noise (Figure 4.4-B).
- Discontinue the experiments if the three-coil probe is overheating.

After considering these precautions in the setup process, assembly of the system can be done. Now to maximize the action of 90^{o} and 180^{o} pulses, the probe will be rotated until the longitudinal axis is perpendicular to zero degrees of a compass (Figure 4.4-C). Furthermore to align the gradient coil with the Earth's field, Maganprobe^{TM}, a 3-axis compass is used to rotate the marked arrow on the gradient coil in the direction of the Maganprobe^{TM} 3 compass as indicated in Figure 4.4-D. For rotation and direction, both should be done accurately to prevent slight deviation which can directly impact the FID signal quality.

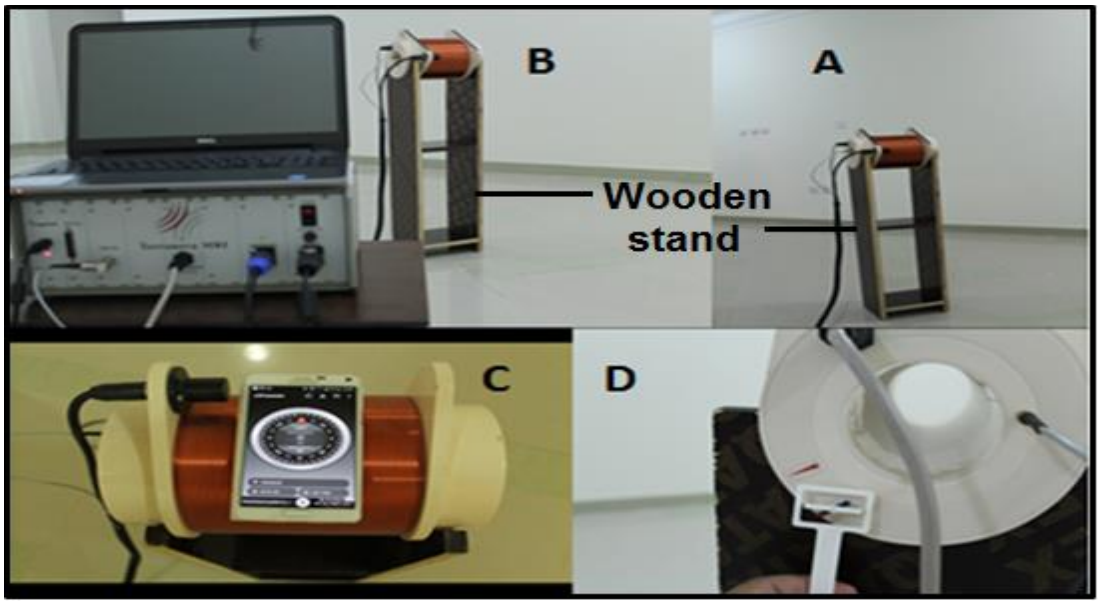

Figure 4.4. A) Shows the probe in wooden stand away from the wall. B) Shows the spectrometers connected with PC and Probe. C) Shows the compass perpendicular with Probe on zero degree. D) Shows MaganprobeTM 3 axis compass aligned with middle coil's marked arrow.

The external noise check feature of the instrument is used to determine the noise level. If the value is bigger than 10 µV rms, the location should be reassessed or changed. If the noise level is less than 3 µV rms, the location is appropriate (Figure 4.5).

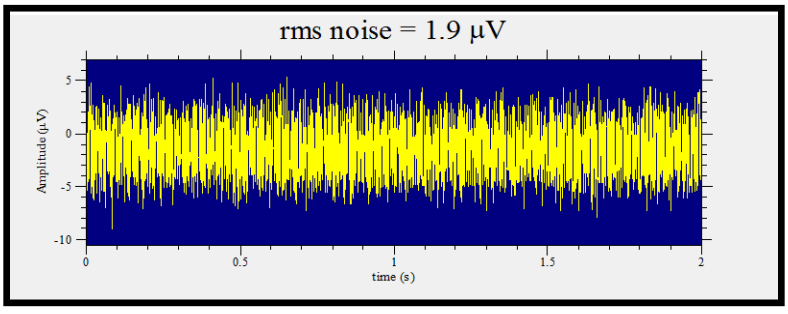

Figure 4.5. Noise level is 1.9 µV rms.

4.4 EFNMR Apparatus versus Conventional MRI device

The main differences between the EFNMR apparatus and a conventional MRI device are:

- The flux density of static magnetic field generated. A conventional MRI instrument generates a huge magnetic field up to 3T (60,000 times of Earth's Field), whereas the EFNMR apparatus generates maximum 18.78 mT (350 times of Earth's Field).
- The homogeneity in the magnetic field of conventional MRI units is not easy to disturb, while in EFNMR apparatus is easy to disturb.
- The Larmor frequency for the EFNMR apparatus is dependent on the location of experiments in the world, unlike conventional MRI.
- The dominant static magnetic field in EFNMR apparatus changes from Polarization pulse to Earth's field. In other words, two T_1 values shall be measured: T_1 in the Earth's field, and T_1 in the polarizing field. The dominant static magnetic field in conventional MRI scanners is the same in the excitation and detection stages. Therefore, one value for T_1 exists.

4.5 Chapter Summary

The main parts of the EFNMR apparatus are: a three-coil probe, a spectrometer, and Prospa software. The three-coil probe directions are designated to be**:** the Z-axis,

which is always along the Earth's Field direction, the X-axis, with a direction along the coil axis, and the Y-axis, which is perpendicular to both axes.

The main experimental parameters for NMR (polarizing currents, B1 frequency, capacitance, transmit gain, pulse duration, receive gain, repetition time, and number of scans) and MRI (dimension, orientation, matrix size, field of view, phase gradient duration, echo time, and bandwidth) are listed and described in this chapter.

Standardization of the instrument setup and precautions was done to avoid any discrepancies in the experimental results since the homogeneity in the magnetic field of EFNMR apparatus is easy to disturb. Upon successful installation and parameter selection, the experiments can be started. The details of the experiments for NMR are described in the following chapter.

5 NUCLEAR MAGNETIC RESONANCE EXPERIMENTS

This chapter presents a series of Nuclear Magnetic Resonance (NMR) experiments and demonstrates how the Free Induction Decay (FID) signal is acquired and how the NMR parameters are tuning. The relaxation time and the process of shimming are also discussed. Some examples will be presented for FID and NMR signals which did not follow precautionary measures during testing. These include inaccurate probe orientation, magnetic field inhomogeneity, and variation of water volume.

5.1 FID Acquisition and Tuning of NMR Parameters

Acquiring a FID signal is the most challenging part in these experiments. To obtain an exponentially decaying FID signal with a strong narrow peak in the spectrum from the first trials is not straightforward, and finding the underlying reasons is a challenge especially for a novice user. A phantom with 500 ml tap water is placed inside the probe apparatus. The FID experiment will be run by using the *Pulse and collect dialog* under the drop menu of EFNMR macro in Prospa (Figure 5.1).

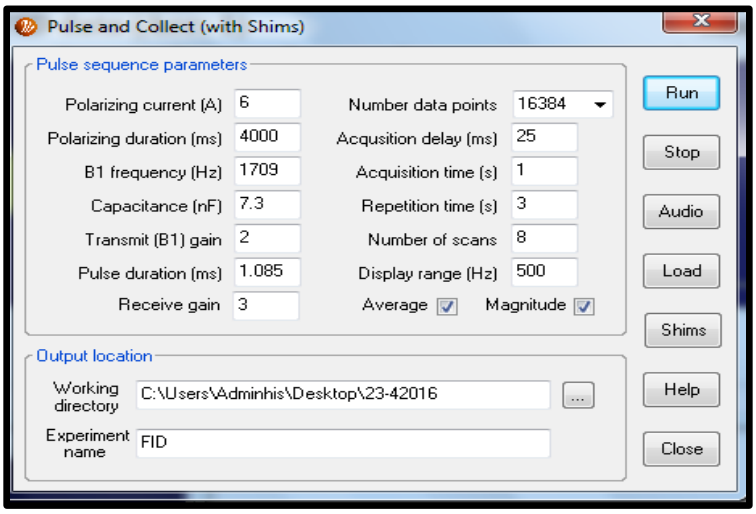

Figure 5.1. Pulse and Collect dialog interface.

It is a challenge to distinguish whether the collected signal is noise or a FID. To confirm the signal is FID, the tap water can be removed and the experiment repeated. If the spectrum is different in both cases, this means the signal obtained is a FID signal. Otherwise, the Probe should be reoriented and changed to a new location. Moreover, the FID signal could decay quickly. The acquisition time needs to be decreased and the Probe might need reorientation and relocation. If the FID signal is not appearing, the Larmor frequency and capacitance values should be re-estimated. If still no FID signal appears, another helpful solution is to perform another series of measurements by changing the two values (frequency and capacitance). The value of capacitance is initially calculated by using the Larmor frequency and resonance (was described in the previous chapter) where the Earth's magnetic field and the gyromagnetic ratio for the hydrogen nucleus are known. To be more accurate, the Earth's field data for Qatar was found in [37] and is

used in these computations. The value of the Earth's found in [37] is 43.6 μT.

If an exponentially decaying FID signal is still not obtained, it will help if the B_1 pulse duration and transmit gain are changed to maximize the FID signal. The duration of B_1 is obtained by using macros in Prospa with the results shown in Figure 5.2. The maximum value for a 90^o pulse duration is 1.085 ms and the minimum value for 180^o pulse duration is 2.17 ms. (Figure 5.2). In case the signal is not obtained at all, the experimental environment needs to be changed and all mentioned procedures should be repeated again.

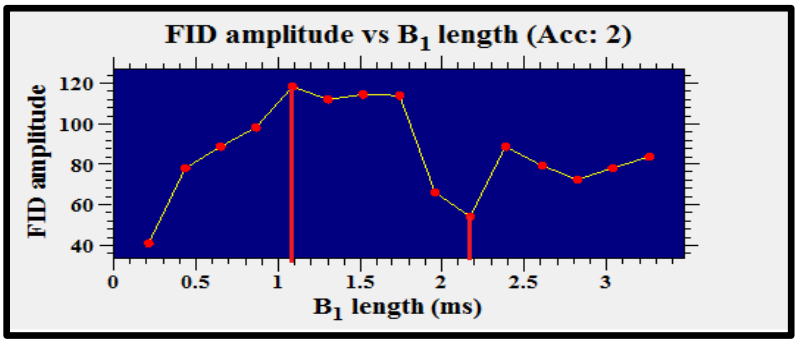

Figure 5.2. The first vertical line shows the maximum value, which is the value for 90o pulse duration and the 2nd vertical line for minimum value, which is the value for 180o pulse duration.

After an acceptable FID signal is acquired the next step is to improve the quality of the FID signal. This is done by adjusting the capacitance value, in order to have B_1 resonance matched to the Larmor frequency of the sample. The coil ring-down decay signal should be detected by shortening the acquisition delay time. The Fourier

Transform for the coil ring-down signal is like a sinc function where the resonance frequency is at the center of the sinc function. Therefore, the capacitance value is controlled by the Prospa until the narrow spike NMR signal is at the center of the coil ring-down signal (Figure 5.3).

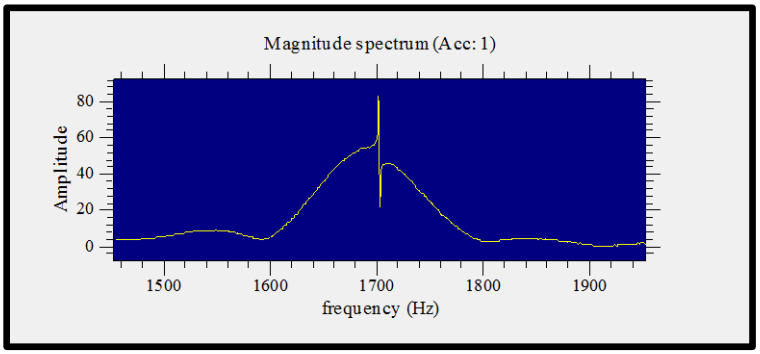

Figure 5.3. FID signal in frequency domain after tuning of NMR Parameters.

Figure 5.4 shows a FID signal with eight scans, acquired after tuning of NMR Parameters.

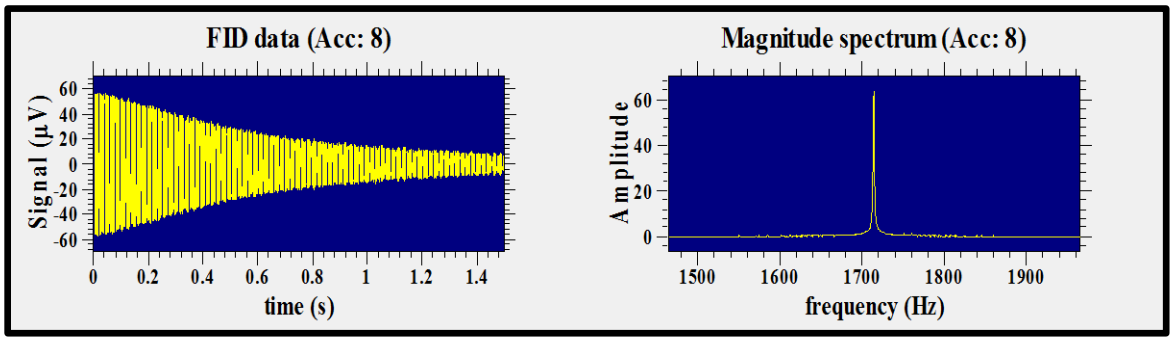

Figure 5.4. FID signal in time and frequency domain starting decay from 56 µV.

5.2 Shimming

Naturally, the Earth's field is highly homogeneous. On the other hand, it is very weak and can be easily disturbed by any external sources like ferrous or low-frequency sources. The shimming option should be used to fix the magnetic field inhomogeneity and improve the quality of the NMR signal. Shimming works by passing a small current through the designed coils in order to create a weak magnetic field to cancel out the underlying inhomogeneity of the static field (Figure 5.5).

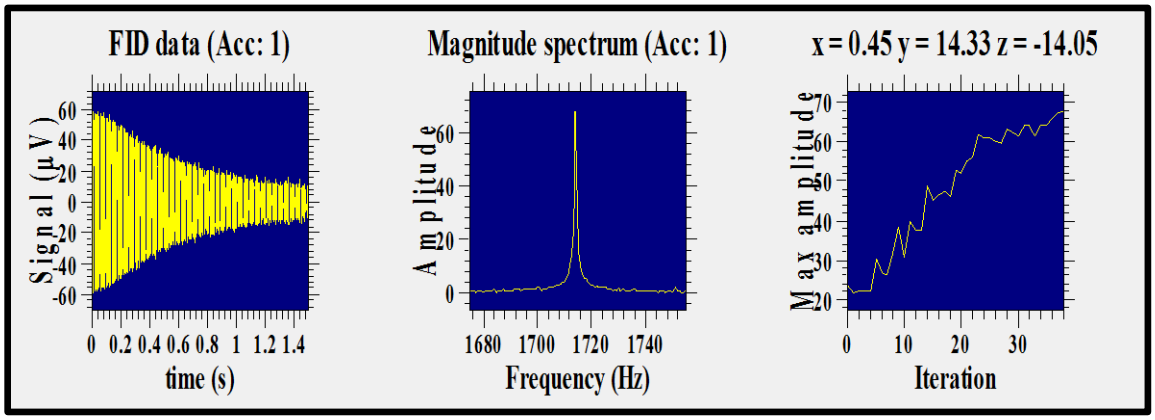

Figure 5.5. The rightmost graph shows the history of the shimming process. This procedure takes at least 7 minutes.

5.3 Measuring T_1

As mentioned in Chapter 3, there are two T_1 values that exist, one in the polarization field and one in Earth's Field. Measuring T_1 in the polarizing field is achieved by using the T_1 macros dialog in Prospa, a series of experiments with different

polarized pulse duration will be conducted. This will be controlled by the polarization step size, number of steps, and minimum polarizing time. During the polarization pulse, the nuclear magnetization will be established and grown. In this stage, the time constant T_1 is related to spin-lattice interaction (Figure 5.6).

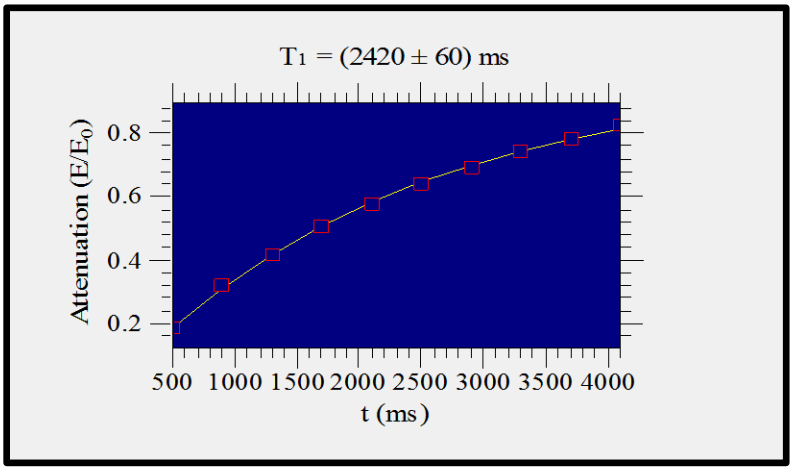

Figure 5.6. T_1 data for each new polarization time. A 500 ml tap water is used. The T_1 in the polarization pulse Field (Bp) is 2.42 s in this case.

The Earth's magnetic field starts after the polarization field is turned off. This equilibrium magnetization will align with the Earth's magnetic field and start to relax. To measure T_1 in the Earth's magnetic field, each read point should be captured with variable delay time between the polarizing and 90° pulses (Figure 5.7).

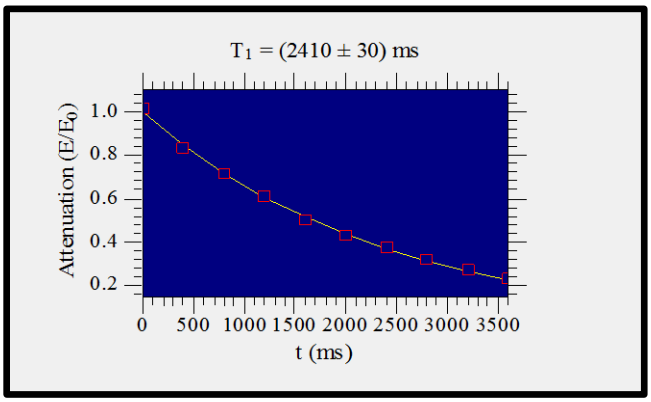

Figure 5.7. T_1 in the Earth's Magnetic Field (BE), T_1 is 2.41 s in this case.

5.4 Measuring T_2

In the event where the magnetic field is not steady and uniform, as most of the cases are, and after the application of the 90° RF pulse, different Larmor frequencies appear as different magnetic field are applied on different spins. Therefore the spins will out-phase in a much shorter time termed T_2*. In case where the magnetic field is steady and uniform, where it rarely occurs, and after the 90° RF pulse is already applied, the signal will be observed as a function of time T_2.

To measure T_2 accurately, shimming and spin-echo pulse are needed to refocus the de-phasing related to the magnetic field inhomogeneity. By using the T_2 macros dialog in Prospa, the echo times are auto incremented for each experiment. For T_2 the echo amplitude decays exponentially as a function of time (Figure 5.8).

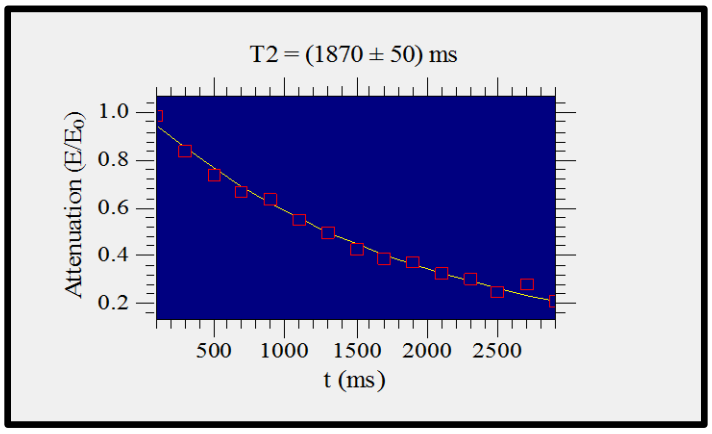

Figure 5.8. T_2 measurement is 1.87 s.

5.5 Carr-Purcell-Meiboom-Gill (CPMG) Experiment

To increase the accuracy of T_2 measurement, a train of spin-echo pulses can be used. A signal decays weighted by T_2^* due to the de-phasing that occurs because of the inhomogeneous magnetic field. Using a train of 180^o RF pulses will correct the de-phasing and the signal will decay weighted by T_2. This method is very sensitive for the pulses' accuracy. If the 180^o RF pulse duration is more or less than the ideal 180^o RF pulse duration, it will lead to accumulative error. That means the error in the last echo actually is the error caused by previous pulses (Figure 5.9).

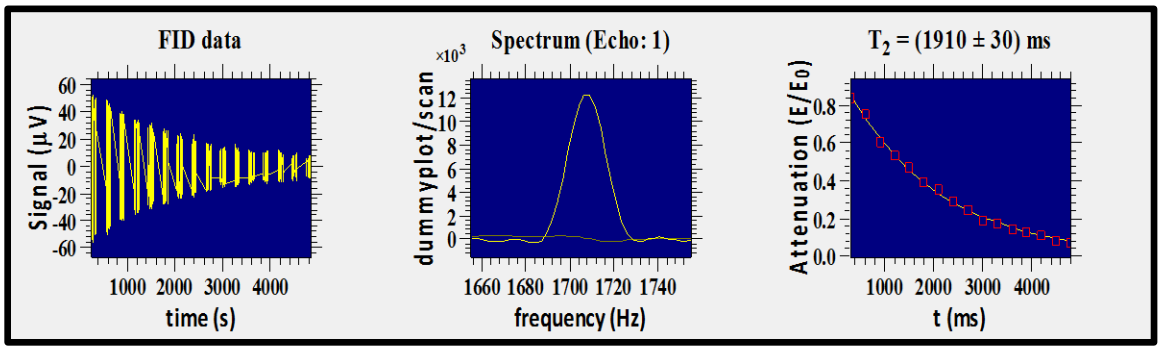

Figure 5.9. The FID signal weighted by T_2 using CPMG pulse sequence in time and frequency domain. T_2 is 1.91 s.

5.6 FID and NMR signal Examples with Poor Quality

This part will present some examples for FID and NMR signals which did not follow precautionary measures during testing. An example of a bad quality FID signal is shown in Figure 5.10 where the three-coil probe contains inaccurate orientation and the magnetic field inhomogeneity is significant.

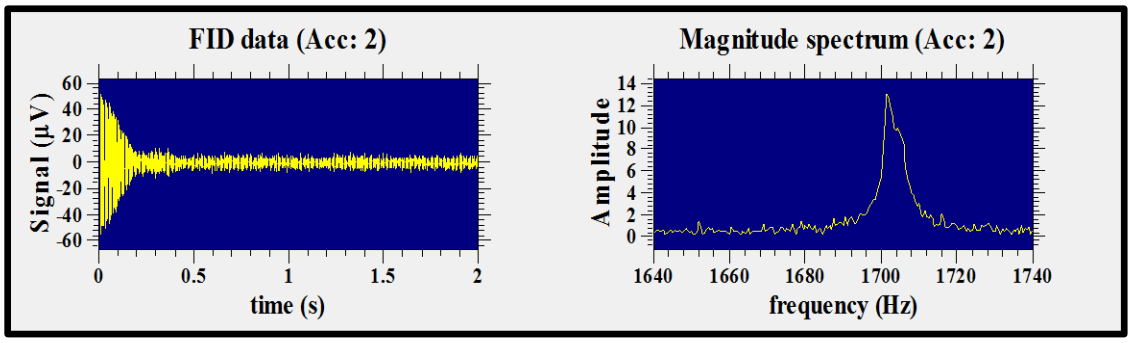

Figure 5.10. An example of short FID signal in time domain due to inhomogeneity in magnetic field. The NMR spectrum is showing broad peak.

Another example explores the effect when items containing metal are placed near the probe. As shown in

Figure 5.11, the FID signal decayed quickly after moving some metal chairs around the Probe. Thus, it decreased the magnetic homogeneity.

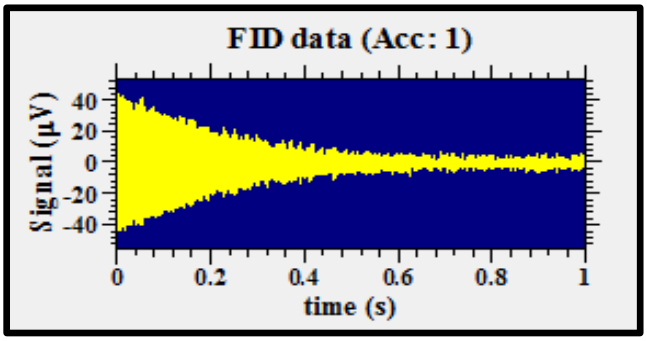

Figure 5.11. An example of FID signal without shimming.

Figure 5.12 and Figure 5.13 show the effect in FID signal when water volume and water state are changed.

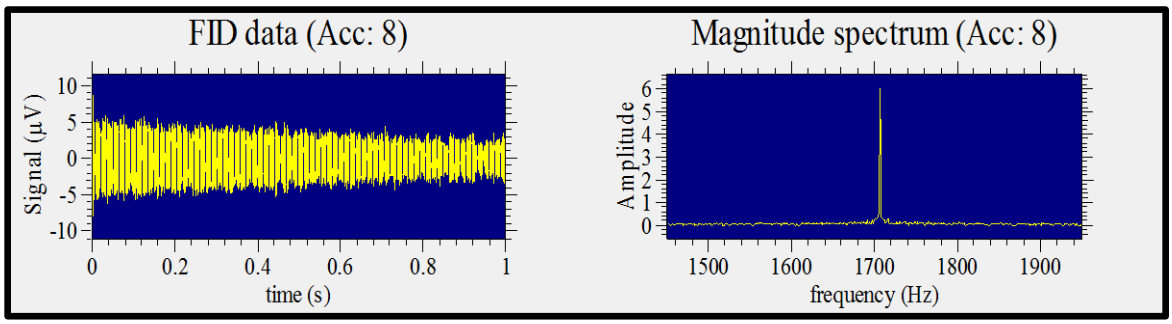

Figure 5.12. An example of FID signal in time and frequency domain for 35 ml water.

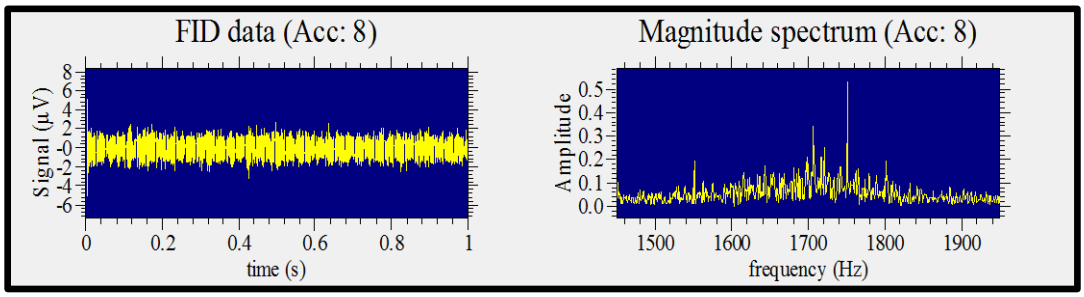

Figure 5.13. An example of FID signal in time and frequency domain for 64 ml iced water.

If the sample or object of interest is changed, the entire NMR signal values will change too. For instance, T_1 measurements for water in B_p and B_E were 2.42 s and 2.41 s respectively, whereas the T_1 measurements for cook oil in B_p and B_E were 0.09 s and 0.18 s respectively. Therefore, all experiments were done on water to guarantee that the hydrogen nuclei mobility is the same consequently all NMR results are same.

5.7 Discussion

The EFNMR does not utilize any large magnetic fields (350 times of Erath's magnetic field), so the hazard of a large magnet is not there. On the other hand, disturbing the magnetic field homogeneity is easy, this is why the shimming process is important to fix the magnetic field inhomogeneity, and could be repeated many times during the experiments. This procedure takes 7 min. The EFNMR apparatus is sensitive for many factors like: the Probe location, orientation, internal overheating, and variable experimental parameters need to be adjusted. The most difficult experiment was

acquiring the FID signal. To obtain the FID, the following have to be fulfilled:

All mentioned timing in this section is varying from user to another user, based on the user experience.

- The noise level has to be less than 3 μV. Four different places were tested to find a place with a noise level less than 3 μV. In some places the noise level exceeded 10 μV. This procedure takes short time, less than one minute.
- The Larmor frequency and the capacitance should be 1709 Hz and 7.3 nF for the particular location where the EFNMR instrument was installed. This procedure takes up to 10 min.
- The probe orientation should be accurate. This procedure takes 5-7 min.
- All *pulse and collect* dialog parameters should be adjusted correctly. This means that the maximum value for a 90^o pulse duration is 1.085 ms and the minimum value for 180^o pulse duration is 2.17 ms. These values are so since the effect of RF pulses with a tip angle of 90^o yields the maximum signal and a tip angle of 180^o pulse yields the minimum signal. This procedure takes 4 min. After adjusting the above parameters the shimming process has to be performed again.

In measuring T_1, there are two T_1 values that exist, one in the polarization field and one in the Earth's Field. During the polarization field, as the polarization pulse duration increases, T_1 increase as well. Once the polarization field is turned off, the Earth's magnetic field starts. The enhanced bulk magnetization related to the polarization

pulse will start to decrease. If the 90^o pulse is used without delay after the polarization pulse is turned off, the highest T_1 value will be obtained. As the delay is increased, the T_1 value will decrease. In measuring T_2, the accuracy of the measurement depends on the magnetic field homogeneity. This is why the shimming and spin-echo pulse are needed to refocus the de-phasing that happens because of the magnetic field inhomogeneity. T_2 measurement was 1.87 s.

5.8 Chapter Summary

In order to obtain a FID signal with exponential decay, the EFNMR apparatus should be placed in a location with a noise level of less than 3 μV rms. The probe orientation should be adjusted accurately and the shimming procedure should be done. The relaxation times that will be used in MRI experiments in Chapter 6 are calculated here. The T_1 in the polarization pulse Field (Bp) is 2.42 s and the T_1 in the Earth's Magnetic Field (BE) is 2.41 s. The T_2 measurement is 1.87 s.

There are two challenges encountered: difficulty in finding the location with noise level less than 3 μV, and the long procedure for shimming (exceeded 7 min for each) and other experimental setups. The total time of experimental setup is at least 30 min. Some examples of experiments that did not consider some precautionary measures in obtaining FID signal are discussed in the last section of this chapter.

The following chapter will demonstrate a series of MRI experiments in preparation for locating distal holes and study relaxation time and imaging contrast.

6 EFNMR-MAGNETIC RESONANCE IMAGING EXPERIMENTS

This chapter presents a series of imaging experiments that have been carried out using the radiation-free MRI technique of Earth's Field Nuclear Magnetic Resonance (EFNMR). A modest femur model has been made to allow simulation of experiments as it is on the real bone.

6.1 Common Experimental Setup

This section discusses the procedures that are followed for each single EFNMR-MRI experiment. Although there are some differences, this procedure was followed in all imaging experiments. The steps are listed below:

- Setting up of all precautionary measures (as described in Chapter 4) prior to the start of any experiment.
- Use of 500 ml tap water to set all experimental parameters.
- Shimming.
- Tuning of the NMR parameters.
- Measurement of the length of 90^o and 180^o pulses.
- Setting up of common field parameters in the common parameters dialog (

- Figure 6.1). All these parameters are explored in Chapter 4 and 5.

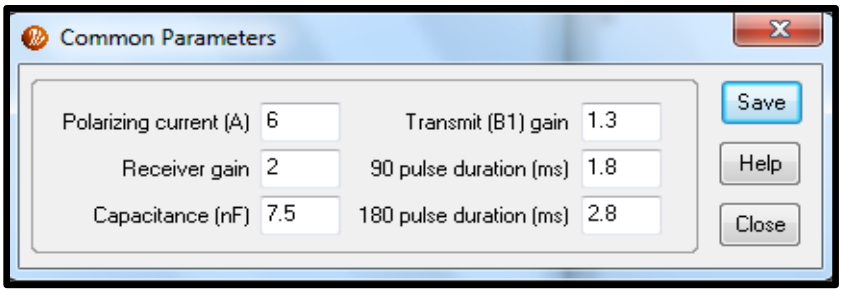

Figure 6.1. The common parameters for all MRI experiments.

6.2 Magnetic Resonance Imaging in 1-D:

In these experiments, the MRI magnetic field gradients and different orientations are explored. The procedure of these experiments can be seen in Appendix [A.1]. In the first experiment, two graphs in 1-D are presented in Figure 6.2. The right and left graphs are captured along the Z-axis and X-axis respectively. It appears that the shapes of two graphs are not the same. This is due to the object view along the axes.

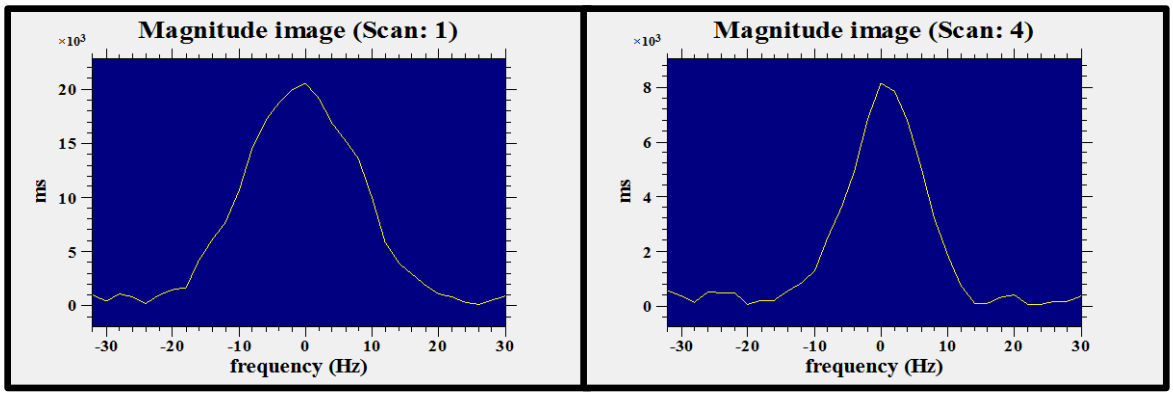

Figure 6.2. Two examples of 1-D. The right graph was taken along the Z-axis. The left graph was taken along the X-axis.

In the second experiment a two-compartment tube inside a bottle. Each compartment is separated from each other and can be filled with 50 ml fluid each. Outside the compartments another volume of fluid can still be added to fill it. The graph in Figure 6.3 is captured along the Z-axis.

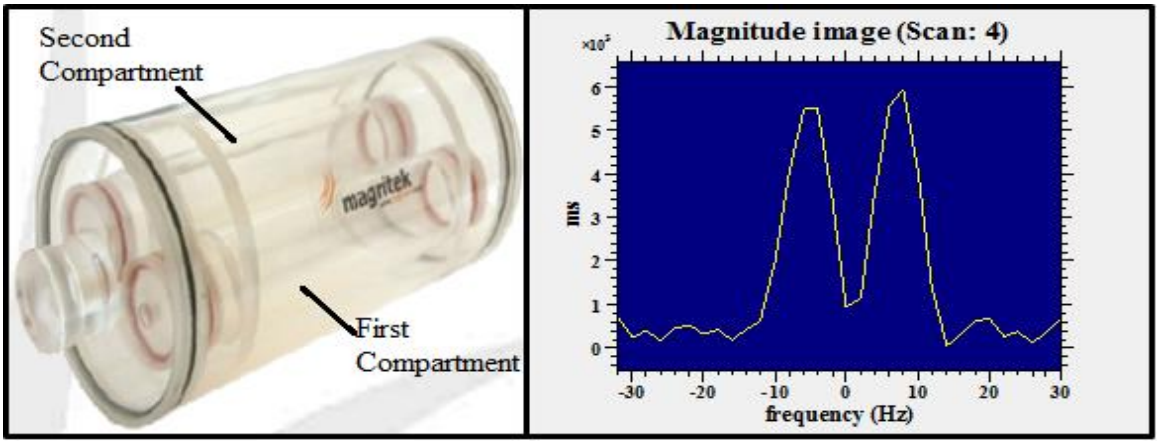

Figure 6.3. Two-compartment tube (left), and 1-D along Z-axis (right).

6.3 Magnetic Resonance Imaging in 2-D: gradient-echo imaging

The principle of phase encoding is applied in this experiment. The gradient echo pulse is utilized to refocus the effect of inhomogeneity in the static magnetic field on spin phase. Start the setup process using the common procedure. Using the same menu dialog that was used in 1-D, select the 2-D option. There are differences in 2-D like image orientation, matrix size, and FOV. The image orientation will provide 6 options. Each option consists of two letters, for example YX. The first letter, which is Y in this case, denotes the direction of the read gradient. The second letter, X, denotes the direction of the phase gradient.

The experimental interface will show the K-space data and the 2-D image. In a 2-D image as described in Figure 6.4, the parameters used can be seen in Appendix [A.2]. Three factors affect the experiments time Eq (5), [33, 35].

$$\text{Experiments time} = \text{RT} \times \text{Np} \times \text{Nscan} \qquad (5)$$

where:

- RT: is the repetition time for each scan, it is recommended to be twice of polarization time duration to avoid the probe overheating.
- N_P: is the matrix size.
- N_{scan} : is the number of scan.

This experiment is acquired with one scan and takes 4 minutes and 16 s.

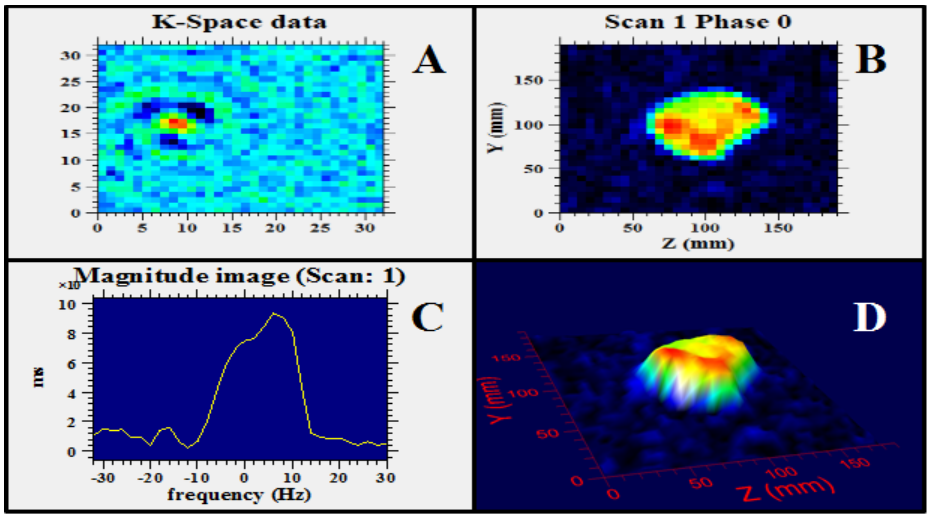

Figure 6.4. A) The K-space data with matrix size 32 x 32. B) 2-D Image using GE-imaging with 180 mm FOV. C) I-D image. D) Another display mode for image which is called surface plot.

6.4 Magnetic Resonance Imaging in 2-D: spin-echo imaging

In this experiment, the image will be shown in 2-D using a spin-echo imaging pulse sequence. The spin echo pulse acts like the gradient echo pulse that refocuses the lost spin phase related to the static magnetic field inhomogeneity. Furthermore, it also refocuses any effect related to the magnetic field gradient. This happens when an 180^{o} pulse is applied. The procedure of the experiments can be seen in Appendix [A.3]. As shown in Figure 6.5, a 2-D image is obtained via spin-echo. This experiment is done for eight scans and lasts for 34 min and 8 s.

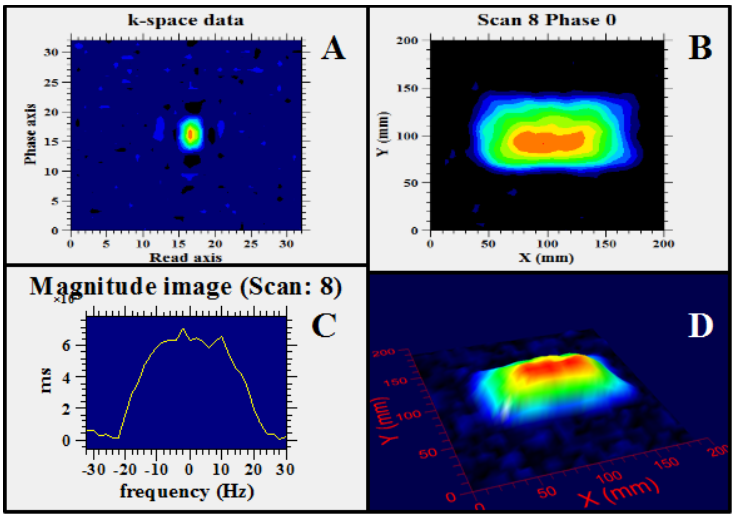

Figure 6.5. A) Shows the K-space data with matrix size 32 x 32. B) 2-D Image by using Spin-echo imaging by changing the display mode to interpolated plot, the FOV is 200 mm. C) Shows the I-D image. D) Another view by using surface plot image.

6.5 Model for Testing

A simple model representing the human femur was developed in order to simulate the real femur. This model consists of:

- A titanium nail which is often used in orthopedic surgery (Kanghui Medical, China). The length of the nail is 340 mm and its diameter is 9 mm. The two distal holes have diameters of 5 mm and 7 mm (Figure 6.6-A).
- Artificial right femur with distal canal opening which is made from cortical/soft cancellous bone with a dense external layer and soft internal part [38].
- Fresh beef meat to act as tissue (Figure 6.6-B).
- The nail distal holes, entrances, and exits are closed by a plastic wrap.

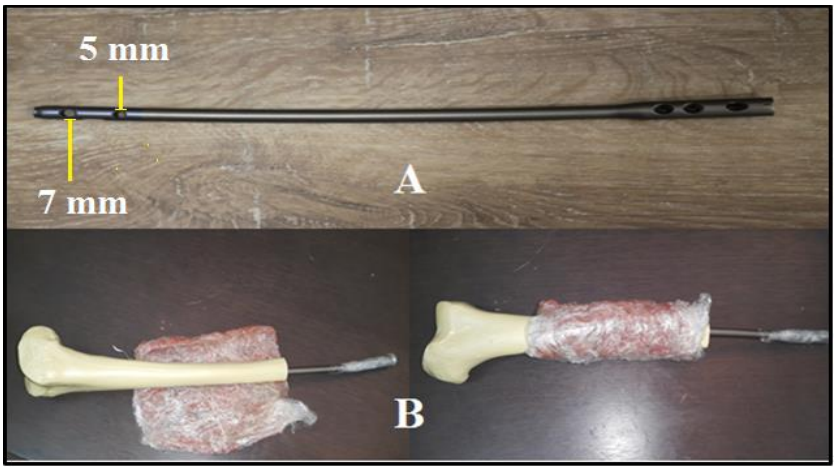

Figure 6.6. A). The IMN and the diameter size of distal holes. B).The nail inserted inside a plastic bone and covered by fresh beef.

The use of fresh beef meat allows working on the contrast factor to distinguish between the meat (tissue) and the water injected inside the nail. When water is injected, it was observed that its maximum volume is up to 3 ml. This is small compared with the water volume that is used in the NMR experiments. Figure 6.7 demonstrates an example on how the water could be injected in the nail and how the holes could be closed. The distal exits and the cross-screw holes could be closed by soluble medical plastic and the proximal part could be closed by a one-way valve that allows one-way flow of water.

The idea in this model is to produce an image by showing the injected water map inside the nail. The two points wherein the distal holes could be located are listed below:

1. The distance between the distal holes and the end of nail is known in advance. This advantage will help to locate the hole.

2. The water volume and shape in distal holes is different than the water inside the nail itself. This could produce a different image.

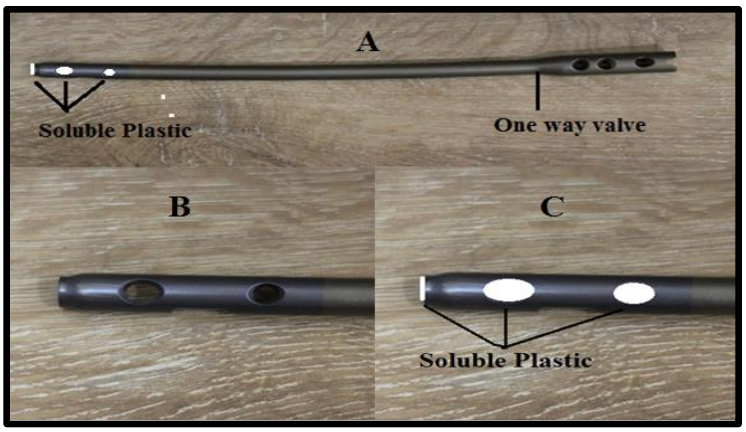

Figure 6.7. Entrance and exits of nail. A) Shows the whole nail with one-way valve, and the place for soluble plastic, B & C) Shows the magnified image of the distal part of the nail before and after placement of soluble plastic.

6.6 Improving imaging efficiency and contrast between regions

There are two problems need to be solved when running MRI experiments:

- Time-consumption. Multi-dimensional images take more time to process. To be efficient, a shorter imaging time is needed to avoid overheating of the probe and more scans could be done to improve SNR.
- No contrast. The modest model was created which needs a contrast between a fresh meat and water.

To improve the visibility between regions of object, a paramagnetic contrast agent, Copper (II) Sulfate ($CuSO_4$) was used in this study. $CuSO_4$ changes the NMR properties by decreasing the relaxation times. In the next sections, the NMR properties are explored to solve the above problems.

6.7 Relaxation time contrast

These experiments investigate how the contrast agents affect the relaxation time constant and how it acts in doped water with different contrast agent concentrations. Finally, it clarifies how the contrast agent can help in reducing the experimental time.

These experiments start the setup process following the common procedure. 500 ml tap water and 500 ml doped water with different $CuSO_4$ concentrations of 500, 1000, 2000, and 4000 µM are used in this experiment (Figure 6.8).

Figure 6.8. CuSO4 powder (159.6 g/mol) obtained from the QU Chemistry Department. By diluting 3.990g in 250 ml distilled water, an amount of 0.1M in 250ml is produced. Every 10 ml, there is 4000 µM.

Table 5 shows the experiment results of T_1 and T_2 for tap and doped water with different concentration of $CuSO_4$ in polarization pulse P_p durations of 1000 ms, 2000 ms, and 4000 ms.

Table 5: Relaxation times in different contrast agent concentrations with different polarization pulse durations

P_p time (ms)	**4000**	**2000**	**1000**	**4000**	**2000**	**1000**	**4000**	**2000**	**1000**
$CuSO_4$ (µM)	**$T_{1\_}B_p$ (ms)**	**$T_{1\_}B_p$ (ms)**	**$T_{1\_}B_p$ (ms)**	**$T_{1\_}B_E$ (ms)**	**$T_{1\_}B_E$ (ms)**	**$T_{1\_}B_E$ (ms)**	**T_2 (ms)**	**T_2 (ms)**	**T_2 (ms)**
0	2400	2100	1800	2340	2070	1800	2000	1850	1700
500	1600	1500	1300	1270	1170	1130	1300	1400	1400
1000	1320	1240	1150	950	900	900	1080	1080	1000
2000	740	730	730	610	603	580	720	700	680
4000	315	316	305	280	280	280	300	310	310

Figure 6.9 and Figure 6.10 show T_1 in polarization field and Earth's field respectively and show the T_1 as a function of CuSO4 concentration by using different polarization times. Figure 6.11 illustrates the T_2.

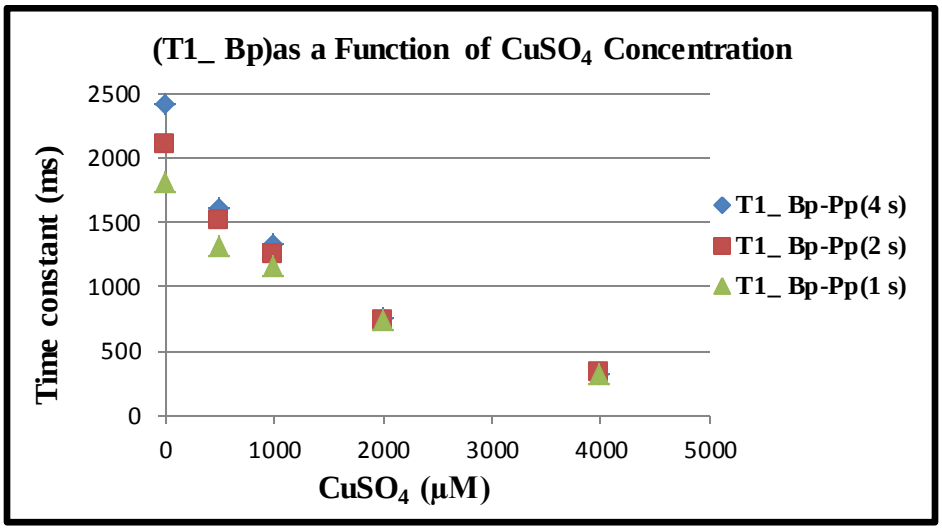

Figure 6.9. The T_1 in polarization field as a function of CuSO4 concentration.

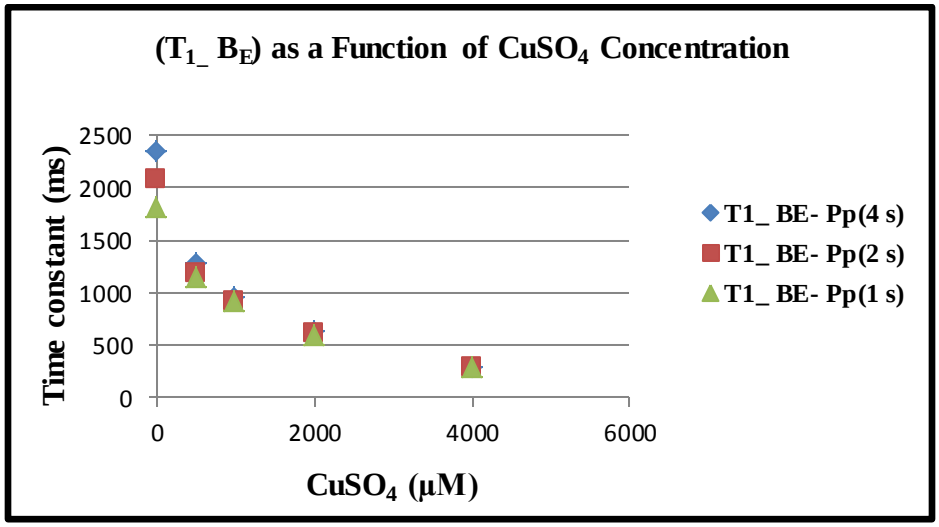

Figure 6.10. The T_1 in Earth's field as a function of CuSO4 concentration.

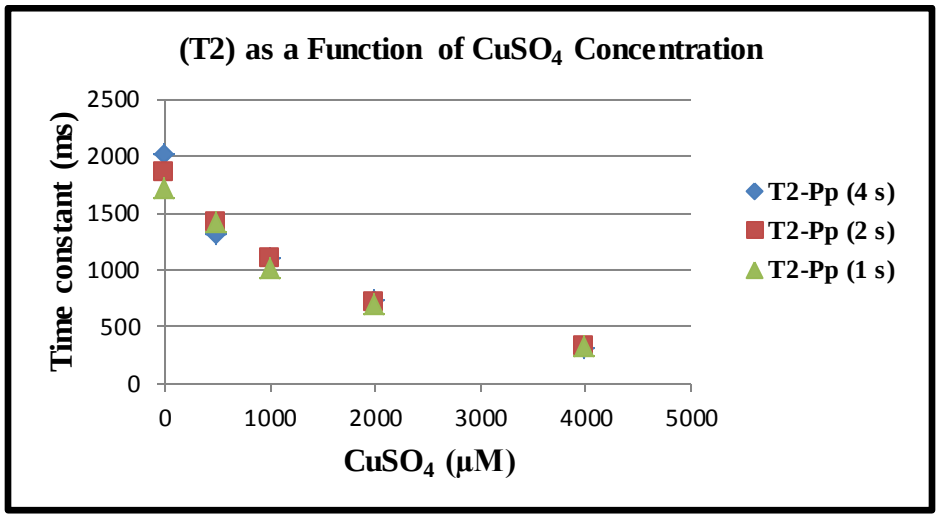

Figure 6.11. The T2 as a function of CuSO4 concentration.

From the above data, the following observations were made:

- Doped water has shorter relaxation times.
- The relaxation time decreases as the contrast agent concentration increases.
- The variation amongst each relaxation time for doped water samples is not significant for all values of polarization times. Either short or long polarization time duration can fully polarize the sample.
- The variation amongst the relaxation times for tap water is significant. Only long polarization times can fully polarize the sample.
- Among all relaxation times, the T_1 in Earth's field is the lowest.

6.8 Relaxation contrast imaging

This section presents how the contrast agent, $CuSO_4$, reduces the experiment time in 2-D MRI, and how it improves the visibility between regions of the object by changing the NMR properties.

Upon completion of the steps in the common procedure, T_2 and T_1 are measured for doped and tap water by using the two-compartment tube. The first compartment tube is filled with 50 ml doped water containing $CuSO_4$ (4000 µM). The second compartment is filled with 50 ml tap water. The experiment is then carried out using different polarization times to see the effect of the polarization time on the image contrast. 2-D images are captured using doped water (with a T_2 equal to 320 ms and T_1 equal to 290 ms) and tap water (with a T_2 equal to 1900 ms and T_1 equal to 2340 ms). In Figure 6.12, four images are captured at different polarization times (400 ms, 1000 ms, 2000 ms and 3000 ms) while keeping the echo time short at 80 ms.

In Figure 6.12-A when 400 ms polarization time is used, the MR image completely appears for doped water, while the MR image for plain tap water is invisible.

In Figure 6.12-B when 1000 ms polarization time is used, the MR image for tap water starts to appear.

In Figure 6.12-C when 2000 ms polarization time is used, the MR image for tap water appears clearer.

In Figure 6.12-D when 3000 ms polarization time is used, the MR image is the same for both samples.

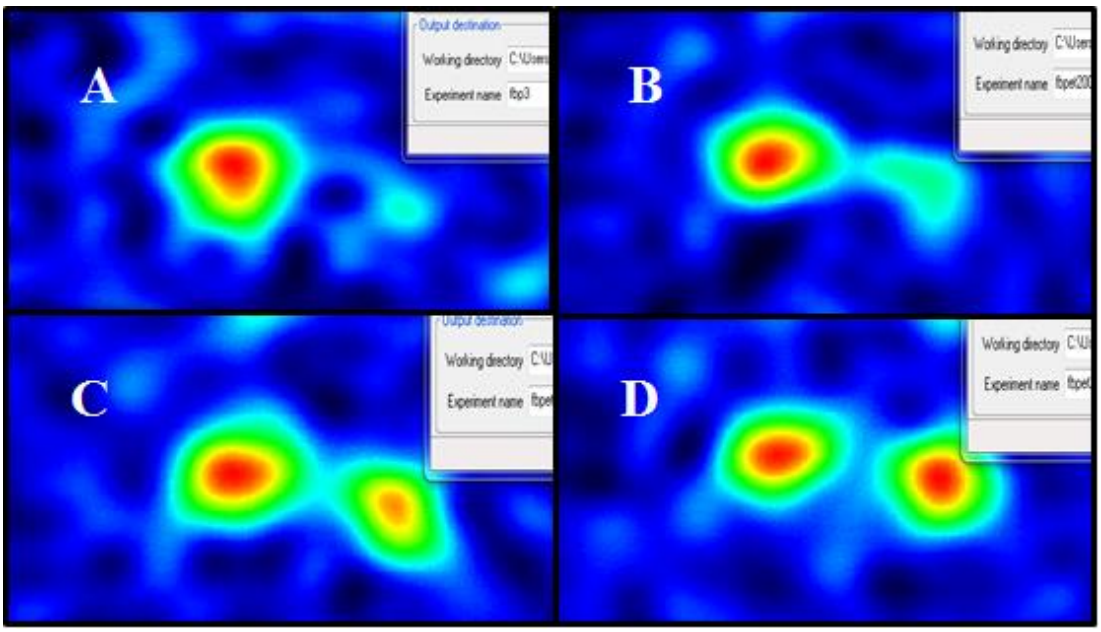

Figure 6.12. Four MR Images are selected in ZY orientation. In all images, the echo time used was 80 ms. A) The polarization time used was 400 ms. B) The polarization time used was 1000 ms. C) The polarization time used was 2000 ms. D) The polarization time used was 3000 ms

The short polarization time fully polarizes the doped water with a short relaxation time but the tap water is partially polarized. As a result, the doped water with short T_1 appears brighter than the tap water with long T_1. It was noted also that when the polarization time is increased, the contrast between both samples is decreased. In long polarization times, both samples are fully polarized and there is virtually no T_1 contrast in image.

6.8.1 Validation of the Contrast Experiment

To validate the contrast concept, each of the tubes in the two-compartment was filled with 50 ml doped water, and then it was submerged in 200 ml tap water Figure 6.13.

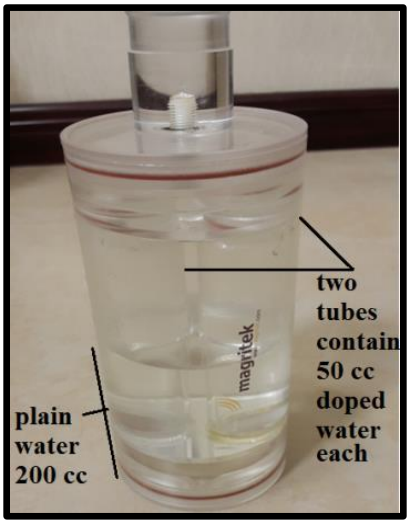

Figure 6.13. Two-compartment tube with each tube filled with 50 ml doped water, and then submerged in 200 ml tap water.

In this experiment, the following parameters are used: polarization time is 400 ms, echo time is 70 ms, t_{grad} is 40 ms, N_p is 32 × 32, RT is 1.5 s, FOV 200 × 200, the number of scans is 4, and the orientation is XY. This image is captured by using spin-echo-imaging.

Images captured in 3 min and 12 s are shown in Figure 6.14. The two tubes are visible in the image but the tap water image disappeared.

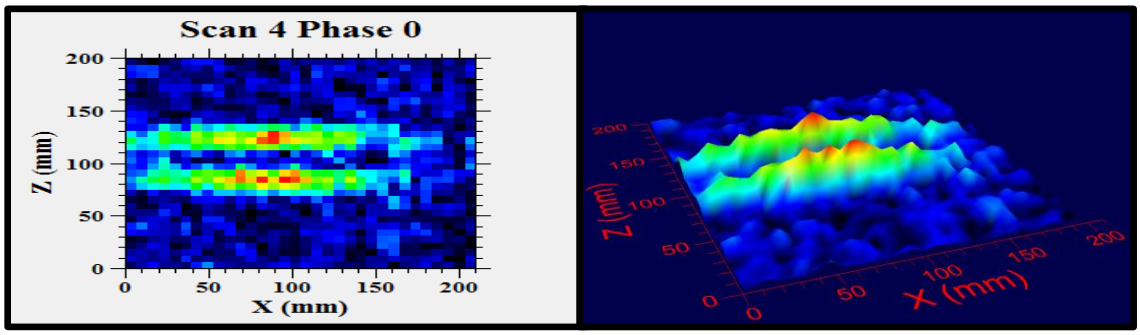

Figure 6.14. Captured MR image wherein the two-compartment tube with doped water are visible and the tap water is invisible. Both images are shown in different display modes.

Two problems have been resolved in this stage—the MRI experiment time and the contrast between regions of interest.

6.9 Detection of small volume of water

Another challenge other than contrast is detecting small water volume. In the experiment where an Intra-Medullary Nail IMN containing a maximum of 3 ml water injected in the probe, the signal cannot be detected. Furthermore, the length of the IMN is longer than the length of the probe. With this, some part of the IMN is outside the probe. Thus, only 1.8 ml water is actually inside the probe making the actual volume lower than 3 ml which makes detection of the signal more challenging.

In order to detect the minimum volume of water that the EFNMR instrument may obtain, a hundred MRI experiments were performed for different volumes of water. Some of the 2-D images are fake images because the MRI is showing some uniform signal as

shown in Figure 6.15. This is usually seen when less than 19 ml of water is used. Appendix B shows two more examples for MR image for low volume of water.

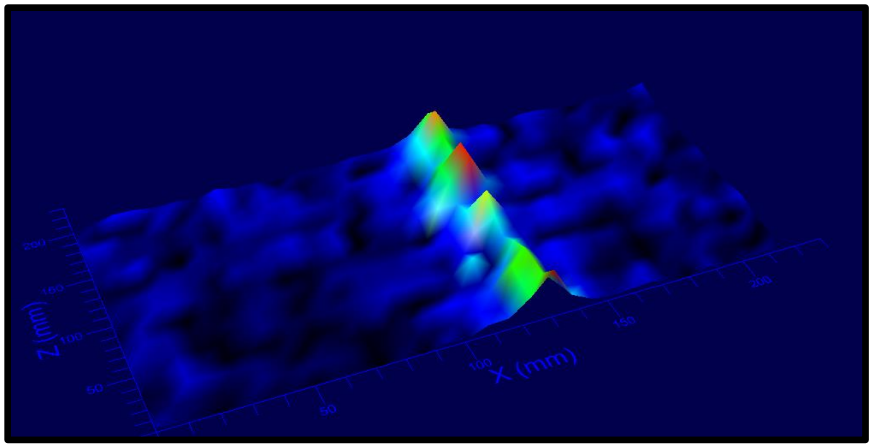

Figure 6.15. MRI without any sample inserted to the Probe.

It was also observed that if there is no visible FID signal, no MR image will be produced. For example, even with weak a FID signal with low noise (less than 3 µV rms), it is possible to produce an MR image. Table 6 shows the relation between the water volume and the FID signal, the amplitude of the signal decreases as the water volume is decreased.

Table 6: The relation between water volume and FID signal

Amount of H2O (ml)	Maximum FID signal (μV)
500	60
50	8
35	6.2
25	5.2
20	3.5
15	2
12	2
10	2

Tables 7, 8 and 9 show how alternating times between long, moderate and short time are affected by the three factors which are: RT, number of scan, and the matrix size. However, when the experimental time exceeds 30 minutes the probe and the sample are overheated.

Table 7: The total experiment time for 2-D MRI with flexible either RT or number of scan and fixed matrix size. The maximum number of scans is 128.

Volume of water (ml)	**MRI-D**	**Polarization duration (ms)**	**Repetition time (s)**	**Number of scan**	**Matrix size**	**Total experiment time (h.m.s)**
500	2-D	4000	8	1	16x16	00.02.08
500	2-D	4000	8	4	16x16	00.08.32
3	2-D	4000	8	40	16x16	01.25.20
500	2-D	600	1.6	1	16x16	00.00.24
500	2-D	600	1.6	4	16x16	00.01.36
1.8	2-D	600	1.5	224 Not Available (NA)	16x16	NA

Table 8: The total experiment time for 2-D MRI with flexible number of scan and with fixed matrix size and RT

Volume of water (ml)	MRI-D	Polarization duration (ms)	Repetition time (s)	Number of scan	Matrix size	Total experiments time (h.m.s)
500	2-D	4000	8	1	32x32	00.04.16
500	2-D	4000	8	4	32x32	00.17.04
3	2-D	4000	8	32	32x32	02.16.32
3	2-D	4000	8	40	32X32	02.50.40
3	2-D	4000	8	112	32X32	07.57.52
500	2-D	600	1.6	1	32x32	00.00.48
500	2-D	600	1.6	4	32x32	00.03.12
3	2-D	600	1.6	32	32x32	00.25.36
3	2-D	600	1.6	32	32x32	00.25.36
3	2-D	600	1.6	80	32X32	01.08.27

Table 9: The total experiment time for 3-D MRI with flexible either RT or number of scan and with fixed matrix size.

Volume of water (ml)	MRI-D	Polarization duration (ms)	Repetition time (s)	Number of scan	Matrix size	Total experiments time (h.m.s)
500	3-D	4000	8	1	32x32x32	02.16.32
500	3-D	4000	8	4	32x32x32	09.06.08
500	3-D	600	1.6	1	32x32x32	00.25.36
500	3-D	600	1.6	4	32x32x32	01.42.24

Figure 6.16 shows a 3-D image for small water volume using two-compartment tube. The first compartment is filled with 50 ml doped water, and the second is filled with 25 ml doped water. This image takes 2 hrs and 50 min.

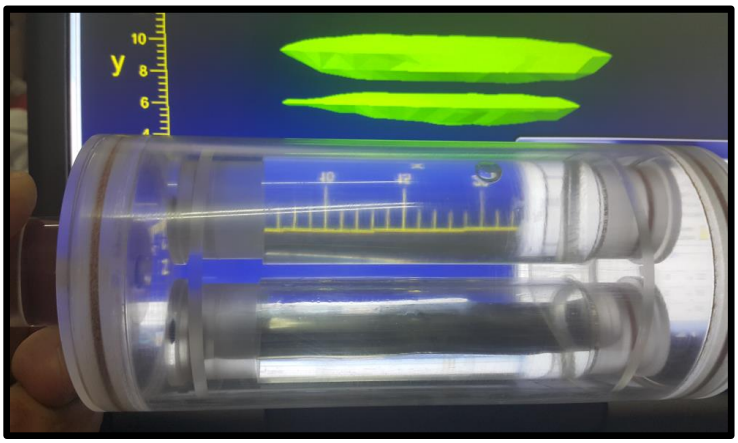

Figure 6.16. The experimental parameters used were: Np = 16 x 16 x 32, polarization time = 500 ms, RT =5 s number of scans = 4. Total experiment time was 02.50.40.

6.10 Proposed solutions to detect small volumes of water

Some experiments have been done to develop a solution to detect a small volume of water in fruits and vegetables based on two reasons listed below:

- Information from Technicians at Imaging Department of Hamad Medical Corporation (HMC): "Some fruits are recommended to be taken by patient prior to MRI procedure. These are oranges, lemons, and pineapples". Also some studies are done for orally administered orange and lemon before MRI and have shown an improved quality in MR images [39].
- The pH level (which is a measure of Hydrogen concentration). The lower the pH (acidic), the higher the hydrogen concentration. Figure 6.17 below shows the concentration of hydrogen at different pH values.

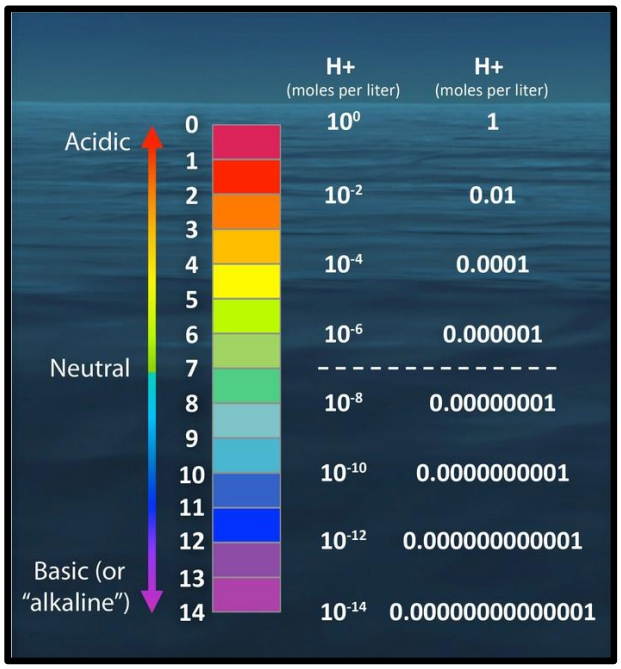

Figure 6.17. The hydrogen concentration (moles/liter) in different values of pH [40].

Examples of food items with approximate pH level values are listed in Table 10 according to the US Food and Drug Administration (FDA).

Table 10: Kinds of fruits and vegetables with approximate pH level [41].

Item	**Approx. pH**
Lemon juice	2.00-2.60
Orange juice, Florida	3.30-4.15
Tomatoes	4.30-4.90
Strawberries	3.00-3.90
Peas, Garbanzo	6.48-6.80
Peaches	3.30-4.05
Beans	5.60-6.50

It can be observed that the lower the range of pH, the higher the hydrogen concentration. For tap water, the pH is within the range 6.5–9.5. On the other hand, a lemon juice (weak acid) has a pH between 2 and 3, which means that the concentration is equal to or more than 1000 µM /L. This difference may be used as an advantage.

A series of FID experiments were taken for different volumes of lemon juice, orange juice, and water to investigate if there will be any improvement. Table 11 below shows that there is no significant improvement in signal amplitude and the decay of signal is very noisy for both juices.

Table 11: Maximum FID signal and different volumes of water, lemon juice and orange juice

Volume of fluid (ml)	**Maximum FID signal (µV) for water**	**Maximum FID signal (µV) for Lemon juice**	**Maximum FID signal (µV) for Orange juice**
30	6	4.5	5.5
20	3	3.5	4
15	2.5	3	2.5

In another experiment where lemon juice is diluted with water in different volumes, it was also observed that there is no significant change. The result is the same in all different lemon juice concentrations (Table 12).

Table 12: The Maximum FID signals for different lemon concentrations

Volume of lemon juice (ml)	Volume of water (ml)	Total volume of mix sample (ml)	Maximum FID signal (μV) for water
5	20	25	5.5
10	15	25	5.5
15	10	25	5.5

Another contrast agent called Gadoversetamide, which is available in hospitals, was tested (Figure 6.18). This agent affects the NMR properties by decreasing the relaxation time. The medical dose is 0.1 mmol/kg (0.2 mL/kg). For testing, different doses of Gadoversetamide are added to different samples with 500 ml of tap water. Results have revealed that even with shimming, improvement of FID signals, and all standard procedures, the FID signal is very weak. The maximum spectrum obtained is only 8 (Figure 6.19).

Figure 6.18. Gadoversetamide ampule is used in real MRI as a contrast agent (0.5 mmol/mL).

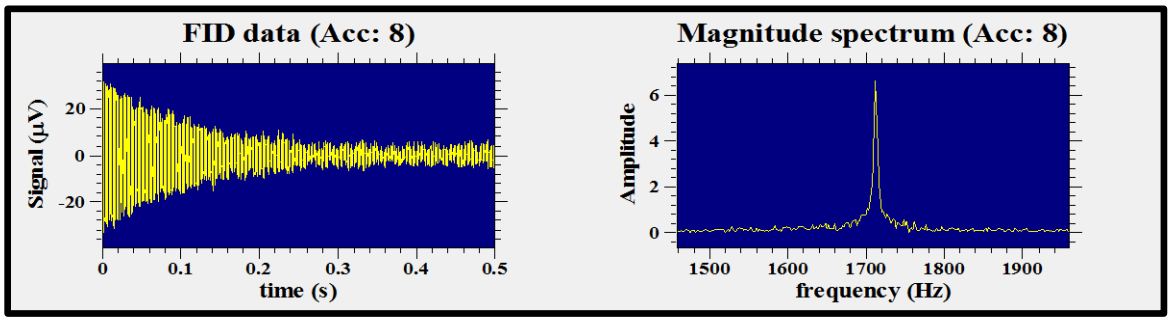

Figure 6.19. The FID signal for doped water with Gadoversetamide. Signal is very weak in doped water as compared with tap water.

Another solution that was considered was to increase the water volume by attaching a strong rubber (like balloon) at the distal end of the IMN as described in Figure 6.20. After inserting the IMN through the medullary canal of femur, water will be injected in the balloon through the nail canal. As the distance is known in advance between the distal nail holes and the end of nail, the location of holes can be detected.

This idea was discussed with two consultant orthopedic surgeons in HMC to know if there is any possibility of reaming the bone marrow (like the ball-socket joint) to inflate the plastic rubber at least by 15 ml to add the same amount of water. Both consultants answered negatively because reaming increases the pressure in the femoral cavity, resulting in embolization which could results in pulmonary embolism. In addition, the width of the bone marrow cavity does not allow for additional reaming.

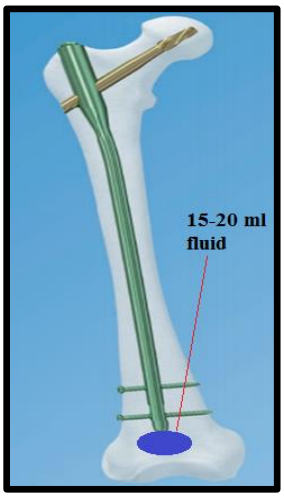

Figure 6.20. Simple demonstration about the idea of attaching a balloon

6.11 Discussion

The main aim of this thesis is to acquire radiation-free images for distal holes in IMN. After a simple model representing the human femur had been built, it was clear that the challenge in this study is to achieve a reasonable contrast between different regions taking into consideration that the fresh meat and water contain hydrogen. Furthermore, the 2-D imaging takes a long time to be performed. If a 2-D image was taken with 4 scans, N_p = 32 x 32 and RT = 8 s, the total experiment time will be 17 minutes. If this experiment is repeated for different image orientations, this will cause overheating of the apparatus and sample. The second challenge is the length of the experiment and its setup time. With MRI, the experiment time increases dramatically.

The contrast agent $CuSO_4$ is very effective in improving the contrast between

regions. It works on NMR properties by decreasing the relaxation time constant by 6-7 times. This gives more opportunities to decrease the polarization time and RT. The RT is usually twice of polarization time. If the RT is long, the experiment will be long as well. Overall, $CuSO_4$ decreases the procedure time and improves the SNR. With this, more scans can be performed. In terms of water volume, it was clear that a volume of water which is less than 19 ml is not enough for producing a FID signal, the following results have been obtained:

- The best amplitude of FID signal obtained in time domain was 60 µV for a large volume of tap water. This is the largest signal that is available in "Qatar" due to its location relative to the strength of the Earth's magnetic field.
- The best noise level recorded is 2.3 µV. So an SNR = 1 will have a peak noise level equal to the rms noise level. This means that any signal less than 2.3 µV cannot be distinguished from noise.

Based on the obtained result the SNR is equal to 60/2.3 = 26. The minimum volume of water that can be detected by a SNR of approximately 1 is equal to 500/26 = 19.1 ml of water. Signal averaging increases the SNR because the signal is coherent and noise is not. The increase in SNR is proportional to the square root of the number of scans [30]. To get down to 3 ml, it would require (19.1/3)^2 = 40 scans in ideal condition. On the other hand, for doped water, the best amplitude of FID signal obtained is 43 µV. To detect 3 ml, 79 scans are required. If the sample volume is decreased to 1.8 ml, more

scans will be required. Practically, all testing is done to detect a signal for 3 ml. Forty (40) scans have been done but only noise is detected. In the case of doped water, experiments become more difficult because the FID amplitude for doped water is 43 μV, whereas the FID amplitude for tap water is 60 μV. Hence, more scans are required.

Three other suggested solutions have been tested to solve the problem in detecting low volumes of water which focus on the following:

1. The pH level and hydrogen concentration in terms of having more hydrogen in a smaller volume. This method has failed, there is no improvement in signal amplitude and the decay of signal is very noisy.
2. Using a medical contrast agent (Gadoversetamide). It has also failed, the best amplitude of the FID signal obtained was 25 μV, whereas the amplitude of the FID signal obtained for tap water and doped water with($CuSO_4$) was 60 μV and 43 μV respectively.
3. Increasing the water volume by attaching a balloon at the end of nail. Two orthopedic surgeons did not recommend this method because it includes the risk of vessels thrombus.

6.12 Chapter Summary

In this chapter, the common experimental setup and parameters for MRI and NMR experiments were established. Many MRI experiments were performed in 1-D and

2-D by using gradient-echo imaging and spin-echo imaging sequences. To simulate the real femur, a simple model representing the human femur was created. This model helped in dealing with challenges related to contrast development between the meat (tissue) and the water injected inside the nail. It was observed that 3 ml is the maximum volume of water that can be injected inside the nail. This is small compared with the water volume that is used in the NMR and initial MRI experiments.

The MRI experiment time and the contrast were resolved by using the contrast agent $CuSO_4$. This improved the visibility between regions of the object by changing the NMR relaxation time where T_2 equals 320 ms and T_1 to 290 ms. The polarization duration which is equal to 600 ms was enough to fully polarize the doped sample with contrast agent. Thus, the experimental time was reduced from 8.32 min to 1.36 min.

After the validation of the contrast experiments, the long MRI experiment time and the contrast between regions of interest have been resolved. Another challenge is how to detect a signal in less than 19 ml of water volume. It was also observed that if there is no visible FID signal, no MR image will be produced. For example, even a small exponational decay of the FID signal with low noise (less than 3 μV rms) is sufficient to produce an MR image. Signal averaging increases the SNR because the signal is coherent and noise is not. Theoretically, for 3 ml of water, 40 scans should be made to obtain a signal. After testing this theory, no signal was detected. All proposed solutions to detect small volumes of water (less than 19 ml) have not worked in this project.

7 CONCLUSION AND FUTURE WORK

7.1 Conclusion

The review of literature for techniques in locating the distal hole in long bone has been done. It has revealed that the standard treatment for long bone fracture is the IMN. The most challenging part in IMN technique is locating the distal hole. Currently, the most popular method is the free hand technique. On the other hand, this technique has a radiation hazard for surgeons and the medical team.

In this study, the radiation-free imaging technique Earth's Field Nuclear Magnetic Resonance (EFNMR) is investigated as an alternative technique to x-rays. A number of experiments were done to understand how the EFNMR apparatus works and to measure the Nuclear Magnetic Resonance (NMR) properties such as the free induction decay signal, and relaxation time.

A simple nail-femur-tissue model was developed to be used in imaging experiments and investigate if the distal holes of the nail can be found. Some problems like contrast between different regions and time-consuming experiments have been encountered but were resolved by using a contrast agent. The result of contrast experiments has shown that there is a contrast between tap water and doped water, and the time of MRI experiments is significantly decreased. At the time where a small volume of sample is tested (less than 19 ml), it was observed that the signal is difficult to

detect.

Since the experiments conducted using the EFNMR apparatus showed that no signal is detected for a water volume of less than 19 ml, three possible solutions have been tested as described below:

1. Using fruit juice where the pH is low and the hydrogen concentration is high.
2. Using medical contrast called Gadoversetamide.
3. Increasing the water volume by attaching a balloon at the end of nail.

All the above-mentioned methods have failed to produce the desirable image. In the first two solutions the amplitude of the FID signal did not increase. The third solution was not recommended by two consultant orthopedic surgeons due to vessels thrombus risk.

In addition to the limitation of the available EFNMR apparatus, which cannot detect signals from a volume of water less than 19 ml, the setup time for the instrument is 30 min, which is long. Furthermore, the Earth's magnetic field homogeneity is easy to disturb. In other words, it may be required to repeat the shimming process which will increase the setup time even more. Eventually, if the location of the EFNMR apparatus (surgery room) is ready with acceptable noise (less than 3 μV) and the instrument is prepared in advance (parameters are all adjusted), 30 minutes will be saved and the image acquisition time will be between 4-16 minutes. Moreover, the current EFNMR apparatus is not practical because the bore has a small diameter and cannot accommodate a human thigh.

Table 13 shows the comparison between the standard technique, which is the free-hand technique, and the EFNMR technique.

Table 13: Free-hand and EFNMR techniques comparison

	Free-Hand Techniques	**EFNMR Techniques**
Preparation time for surgery	Does not need any preparation	Approximately 30 min for instrument setup
Accuracy	Accurate	No data
Exposures in distal locking *(range)*	11 to 81 fluoroscopic images	Ionizing radiation-free
Distal locking time *(mean in min/range)*	The range is 15-55 min including screw insertion	One image required. 1 min and 36 sec with four scans (doped water). The system has not been used in surgery since this is only a proof-of-concept project
Easy to master	Yes	Unknown
Surgeons expertise	Qualified orthopedic surgeon	Qualified orthopedic surgeon
3-D images availability and time required to acquire	Not available	Available. Almost 26 min with one scan

7.2 Future Works and Recommendations

1. To avoid excess surgery time, the EFNMR apparatus has to be setup before the operation. The chosen surgery room has to be shielded from noise and magnetic interference.
2. The current EFNMR apparatus cannot detect volumes of water less than 19 ml. In this application the volume of water that must be detected is 3 ml. When trying to

detect such low volumes of water using the current EFNMR apparatus only noise is recorded, which indicates low SNR ratio. The design of the EFNMR apparatus has to be reconsidered in order to detect volumes of water as low as 3 ml. The strength of MRI signal is proportional to B_o. Eq(6) shows how the longitudinal magnetization (M_L) component is affected by the number of protons (proportional to the volume of water). The B_o field has to be increased in order to increase M_L while keeping the volume of water low (3 ml), [30].

$$M_L = \frac{\gamma^2 \hbar^2 Bo\ N_{total}}{16\pi^2 KT} \qquad (6)$$

where:

- N_{total} is the number of hydrogen protons in 1 ml of water, which is 3.34×10^{23}.
- K is the Boltzmann constant, which is 1.3807×10^{-23} joules per kelvin.
- T is the temperature in Kelvin, which is 300 K.
- B_o is 18.78 mT, which is enough to produce MR image for 19 ml of water.

The M_L for 19 ml water is1.45×10^{-10}. By keeping the M_L constant and at 3 ml of water, the B_o is found 118 mT, which is the least value to produce MRI signal for 3 ml of water. Also the EFNMR apparatus design should consider the dimensions, because the current one cannot be applied around the thigh. The following dimensions are suggested in order to be able to place the apparatus around a normal adult thigh.

- Solenoid length: 50 cm
- Solenoid diameter: 35 cm

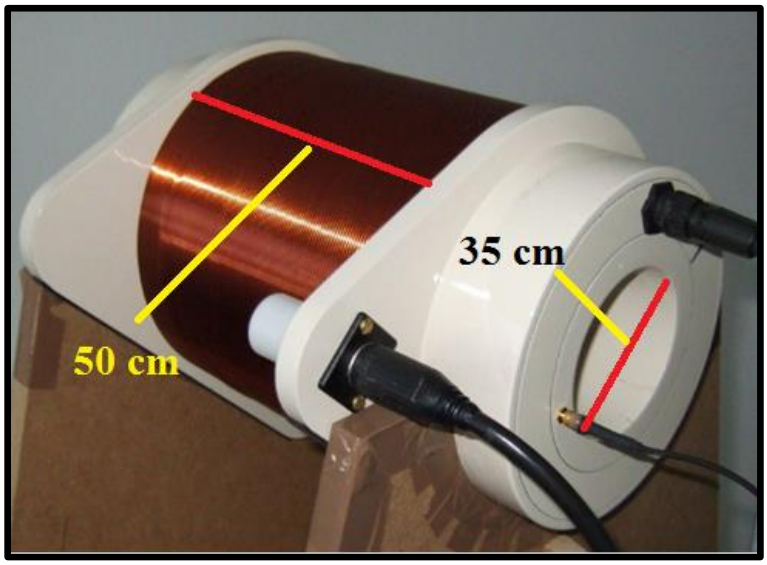

Figure 7.1. The suggestion new dimensions size.

These dimension changes will also affect B_o according to equation (7), [30].

$$B_o = \frac{\mu_o \, n \, I}{\sqrt{L^2 + 4R^2}} \qquad (7)$$

where:

- n is a number of turn.
- I is a current (A), which is 6 A.
- L is a length of the solenoid.
- R is a radius of solenoid.

From this expression the required number of turns for a 6 A current was calculated to be 2441 turns. The magnetic field should be increased with respect to the probe overheating. As the polarization current is limited by the resistive heating within the polarization coil.

3. Extract signals for low volume of water less than 19 ml, and test other signal processing techniques in terms of obtaining an image.
4. For future experiments, in case any solution comes up, when the noise level is more than 10 µV and this is the common case for most places, it is recommended to use an external Faraday Cage (Figure 7.2). The placement of the Probe inside the aluminum shield will help decrease the noise level thereby increasing the SNR. This method is not used in this study since the noise level obtained is already in acceptable value less than 3 µV. Moreover, this method is recommended only for noise levels exceeding 10 µV.

Figure 7.2. The Faraday cage which is made up of 10 mm aluminum sheet with a Probe inside it [35].

5. As an alternative to the EFNMR apparatus, an extremities MRI device can be used. An MRI can capture a complete range of high quality images for extremities as shown in Figure 7.3. It could be used also to detect the distal holes. This device was not tested before since it is not available. The disadvantage of this instrument is its high cost.

Figure 7.3. Extremities MRI [42].

REFERENCES

[1] G. Anastopoulos, P. G. Ntagiopoulos, D. Chissas, G. Loupasis, A. Asimakopoulos, E. Athanaselis, *et al.*, "Evaluation of the Stryker S2^{TM} IM Nail Distal Targeting Device for reduction of radiation exposure: A case series study," *Injury, Int. J. Care Injured,Elsevier,* vol. 39, p. 1210—1215, 2008.

[2] J. F. Barwick and P. J. Nowotarski. (2011, 7 Nov). *Femur Shaft Fractures (Broken Thighbone)*. Available: http://orthoinfo.aaos.org/topic.cfm?topic=A00521

[3] D. A. Becker. (2015, 23 Oct). *A Patient's Guide to Adult Humerus Shaft Fractures*. Available: http://midwestbonejoint.com/fractures/adult-humerus-shaft-fractures/

[4] Botser, I. Busheri, Shapira, Shachar, Herman, and Amir, "Simple Anteroposterior Free Hand Technique for Fast Intramedullary Nail Distal Locking," *Techniques in Orthopaedics,* vol. 26, pp. 119 - 121, 2011.

[5] W. Chu, J. Wang, S.-T. Young, and W. C. Chu, "Reducing radiation exposure in intra-medullary nailing procedures: Intra-medullary endo-transilluminating (iMET)," *Injury, Int. J. Care Injured,Elsevier,* vol. 40, pp. 1084–1087, 2009.

[6] C. M. Court-Brown, *AN ATLAS OF CLOSED NAILING OF THE TIBIA AND FEMUR*. UK 1991.

[7] A. GäNSSLEN, T. GöSLING, F. HILDEBRAND, H. P. PAPA, and H. J. OESTERN, "Femoral shaft Fractures in adults: Treatment Options and controversies," *ACTA CHIRURGIAE ORTHOPAEDICAE ET TRAUMATOLOGIAE ČECHOSL,* vol. 81, pp. 108–117, 2014.

[8] Z. Yaniv and L. Joskowicz, "Robot-Assisted Distal Locking of Long Bone Intramedullary Nails: Localization, Registration, and In Vitro Experiments," pp. 58-65, 2004.

[9] M. X. Kong, Z. J. Du, L. N. Sun, L. X. Fu, Z. H. Jia, and D. M. Wu, "A Robot-Assisted Orthopedic Telesurgery System," presented at the Engineering in Medicine and Biology 27th Annual Conference, Shanghai, China, 2005.

[10] M. R. Bong, K. J. Koval, and K. A. Egol, "The History of Intramedullary Nailing," *Bulletin of the NYU Hospital for Joint Diseases,* vol. 64, p. Numbers 3 & 4, 2006.

[11] B. K. Moor, M. Ehlinger, and Y. Arlettaz, "Distal locking of femoral nails. Mathematical analysis of the appropriate targeting range," *Orthopaedics & Traumatology: Surgery & Research,* vol. 98, p. 85—89, 2012.

[12] ObaidurRahman, R. M. Adnan, R. Khan, F. u. Rahman, M. I. Zia, J. Amin, *et al.*, "Pattern of Femoral Fractures," *Journal of Rawalpindi Medical College (JRMC),* vol. 17, pp. 42-44, 2013.

[13] R. Rohilla, R. Singh, N. Magu, A. Devgun, R. siwach, and A. Gulia, "Nail over nail technique for distal locking of femoral intramedullary nails," *International*

Orthopaedics (SICOT), vol. 33, pp. 1107-1112, 2009.

[14] S. Skjeldal and S. Backe, "Interlocking medullary nails radiation doses in distal targeting," *Arch. OrthopaedicTrauma Surg*, vol. 106, pp. 179-181, 1987.

[15] S. Nakdhamabhorn and J. Suthakorn, "A Novel Surgical Navigation Concept for Closed Intramedullary Nailing of Femur Using 4-DOF Laser-Guiding Robot," presented at the International Conference on Robotics and Biomimetics, Phuket, Thailand, 2011.

[16] S. Nakdhamabhorn and J. Suthakorn, "Design and Development of System Integration for Fluoroscopic Navigation Using Surgical-Guiding Robot," presented at the The World Congress on Computer Science and Information Engineering, 2011.

[17] G. Wang, T. Pan, X. Peng, and J. Wang, "A new intramedullary nailing device for the treatment of femoral shaft fractures: A biomechanical study," *Clinical Biomechanics ELSEVIER*, vol. 23, pp. 305–312, 2008.

[18] C. K. Yiannakopoulos, A. D. Kanellopoulos, C. Apostolou, E. Antonogiannakis, and D. S. Korres, "Distal Intramedullary Nail Interlocking The Flag and Grid Technique," *Orthop Trauma*, vol. 19, pp. 410-414, 2005.

[19] FPR-med. (2015, 7/11). *Ortho Anatomy*. Available: http://www.fprmed.com/Pages/Ortho/FEMORAL_SHAFT_FRACTURE.html#/Pages/Ortho/Ortho_Anatomy.html

[20] S. Salminen, "FEMORAL SHAFT FRACTURES IN ADULTS:

EPIDEMIOLOGY, FRACTURE PATTERNS, NONUNIONS, AND FATIGUE FRACTURES," p. 25, 29 Jan 2005.

[21] C. Krettek, J. MannB, T. Miclau, P. Schandelmaier, I. Linnemann, and H. Tscherne, "Deformation of Femoral Nails with Intramedullary Insertion," *Journal of Orthopaedic Research,* vol. 16, pp. 572-575, 1998.

[22] DoeReport. (2015, 20/12). *Intramedullary Rod: Femur*. Available: http://findlaw.doereport.com/generateexhibit.php?ID=5444&ExhibitKeywordsRaw=&TL=&A=42409

[23] D. S.Chan, R. B.Burris, M. Erdogan, and H. C. Sagi, "The insertion of intramedullary nail locking screws without fluoroscopy: a faster and safer technique.," *J Orthop Trauma,* vol. 27, pp. 363-366, 2013.

[24] T. H. Wong, T. K. Chung, T. W. Liu, H. J. Chu, W. Hsu, P. C. Yeh, *et al.*, "Electromagnetic/Magnetic-Coupled Targeting System for Screw-Hole Locating in Intramedullary Interlocking-Nail Surgery," presented at the SENSORS JOURNAL, Taiwan, 2014.

[25] InnerBody. (2015, 1/11/2015). *Skeletal System*. Available: http://www.innerbody.com/image/skelfov.html

[26] N. P. Rhodes, *Anatomy and Physiology*. UK: Elsevier, 2014.

[27] O. College. (2013). *Types of Fractures*. Available: https://commons.wikimedia.org/wiki/File:612_Types_of_Fractures.jpg

[28] D. A. Becker. (2016, 1 Nov). *Minneapolis Orthopaedics*. Available:

http://www.mplsortho.com/conditions-treatments/ecategory/47/etopic/4e9a2e8d8583ef20c2f7a72ebfa65420/

[29] DePuySynthes. (2012, 23/10/2015). *Titanium Trochanteric Fixation Nail System (TFN)* Available: http://www.synthes.com/sites/NA/Products/Trauma/IntramedullaryNailingSystems/Pages/Titanium_Trochanteric_Fixation_Nail_System_TFN.aspx

[30] N. Smith and A. Webb, *Intoduction to Medical Imaging : physics, engineering, and clinical*. United States, 2011.

[31] A. Webb, *INTRODUCTION TO BIOMEDICAL IMAGING*, 2007.

[32] L. X. George R. Coates, Manfred G. Prammer, *NMR Logging Principles and Applications*. United States of America: Halliburton Energy Services., 1999.

[33] M. E.Halse, *Terranova-MRI EFNMR Student Guide*. Wellington, New Zealand: magritek company, 2009.

[34] R. Dykstra, "THE DEVELOPMENT OF A SPECTROMETER FOR PORTABLE NMR SYSTEMS," PhD, Physics Massey University, New Zealand, 2006.

[35] M. E.Halse, *Terranova-MRI EFNMR User's Manual* Wellington, New Zealand: magritek company, 2009.

[36] Y. H. Carr and E. M. Purcell, "Effect of Diffusion on Free Precession in Nuclear Magnetic Rosonance Experiments," *Physics*, vol. 94, pp. 630-638, 1954.

[37] (1 Feb 2015). *Magnetic Field Calculators*. Available: http://www.ngdc.noaa.gov/geomag-web/#igrfwmm

[38] R. Fritschi. (1988, 8/10/2016). *SYNBONE*. Available: https://www.synbone.ch/wEnglish/catalogue/index.php?navanchor=1010102

[39] Z.-Q. Chu, Q. Ji, and J.-L. Zhang1, "Orally administered lemon/orange juice improved MRCP imaging of pancreatic ducts," *Springer Science+Business Media*, vol. 35, pp. 367–371, 2009.

[40] R. A. Feely. (17/10/2016). *A primer on pH*. Available: http://www.pmel.noaa.gov/co2/story/A+primer+on+pH

[41] U. FDA. (2008). *Approximate pH of Foods and Food Products*. Available: http://www.foodscience.caes.uga.edu/extension/documents/FDAapproximatepHoffoodslacf-phs.pdf

[42] E. SpA. (2016, 11 Nov). *Mobile Medical Imaging* Available: http://www.mobilemedicalimaging.ca/

8 APPENDIX

Appendix A

Appendix [A.1]

After following the common procedure steps, the Gradient- Echo imaging dialog is opened and an experiment for 1-D is initiated (Figure 8.1). In this dialog, the letter of image orientation denotes the direction of the read gradient.

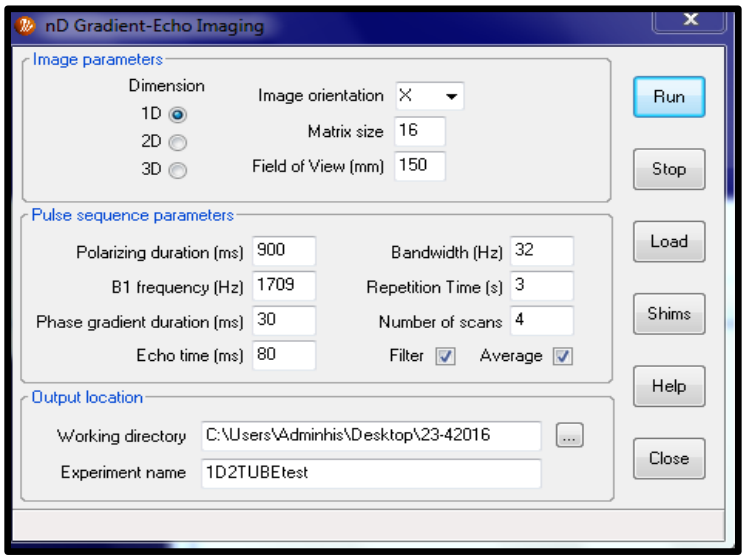

Figure 8.1. Gradient-Echo Imaging dialog under MRI menu in Prospa.

In the examples below the following experimental parameters have been used: t_{Grad} = 270, echo time = 540, $t_{Aca\text{-}delay}$ = 20 ms, polarization time = 4000 ms, matrix size (Np) = 32, and different values of FOV.

Appendix [A.2]

The parameters used are : polarization time = 4000 ms, repetition time (RT) = 8 s. Thus, RT is equivalent to at least the double of the polarization time, FOV = 180 mm, Np = 32 x 32, bandwidth = 64 Hz, t_{Grad} = 30 ms, $t_{Aca\text{-}delay}$ = 20 ms.

Appendix [A.3]

The spin echo imaging dialog (Figure 8.2) is used in this experiment after following the common procedure. One parameter in this dialog differs from the gradient-echo imaging dialog. This is called the phase cycle. In case many successive signal acquisitions occur, the phase cycle contains the manipulation of the radio frequency pulses phase. In such a way, the resultant combination of the desired signal is combined constructively.

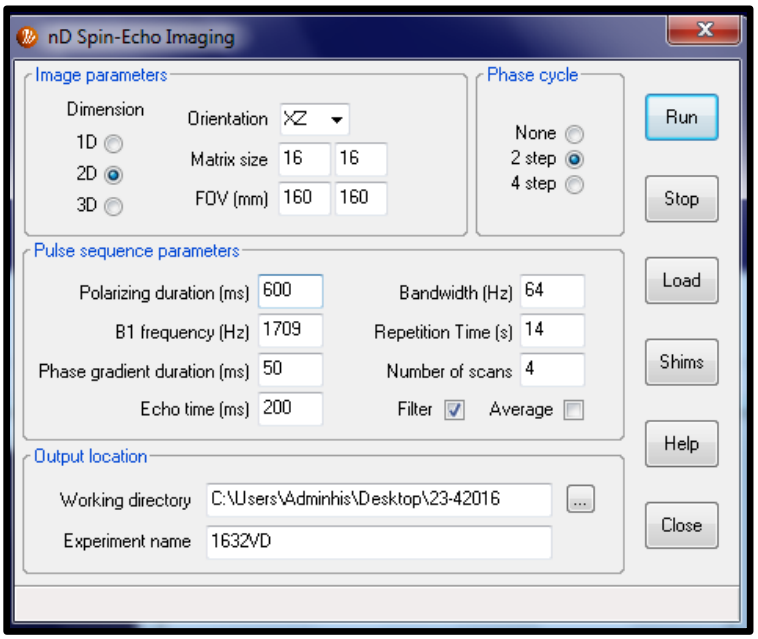

Figure 8.2. Spin-Echo Imaging dialog under MRI drop menu.

Parameters used were: polarization time = 4000 ms, RT = 8 s, FOV = 200 mm, N_p = 32 x 32, bandwidth = 64 Hz, t_{Grad} = 30 ms, $t_{Aca\text{-}delay}$ = 20 ms.

Appendix B

Figure 8.3 and figure 8.4 show an example for MR image with water 5 ml and image without water sample.

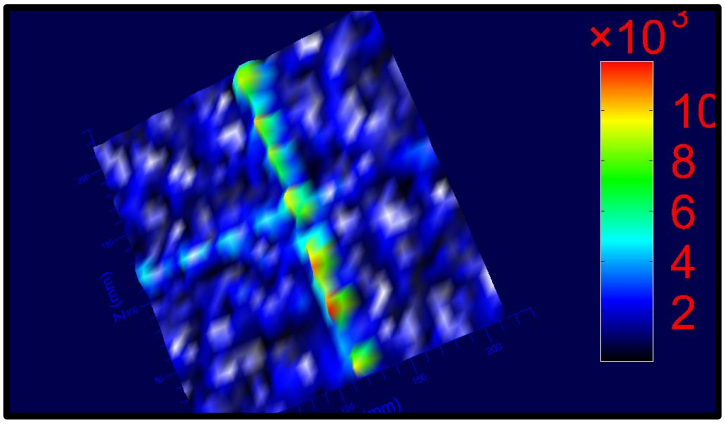

Figure 8.3. MRI with 5 ml water sample inserted to the Probe.

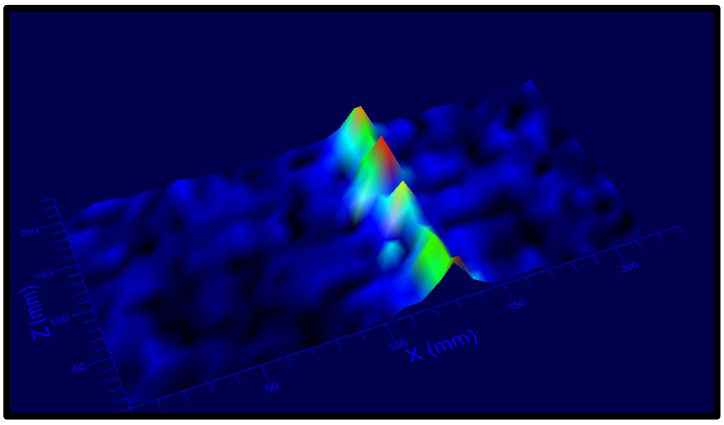

Figure 8.4. MRI without any sample inserted to the Probe.